

Aerodynamic Stall and Buffet Modeling for the Cessna Citation II Based on Flight Test Data

Horssen van, Laurens; de Visser, Coen; Pool, Daan

DOI

[10.2514/6.2018-1167](https://doi.org/10.2514/6.2018-1167)

Publication date

2018

Document Version

Accepted author manuscript

Published in

Proceedings of the 2018 AIAA Modeling and Simulation Technologies Conference

Citation (APA)

Horssen van, L., de Visser, C., & Pool, D. (2018). Aerodynamic Stall and Buffet Modeling for the Cessna Citation II Based on Flight Test Data. In *Proceedings of the 2018 AIAA Modeling and Simulation Technologies Conference: Kissimmee, Florida* Article AIAA 2018-1167 American Institute of Aeronautics and Astronautics Inc. (AIAA). <https://doi.org/10.2514/6.2018-1167>

Important note

To cite this publication, please use the final published version (if applicable).
Please check the document version above.

Copyright

Other than for strictly personal use, it is not permitted to download, forward or distribute the text or part of it, without the consent of the author(s) and/or copyright holder(s), unless the work is under an open content license such as Creative Commons.

Takedown policy

Please contact us and provide details if you believe this document breaches copyrights.
We will remove access to the work immediately and investigate your claim.

Aerodynamic Stall and Buffet Modeling for the Cessna Citation II Based on Flight Test Data

L.J. van Horssen*, C.C. de Visser[†] and D.M. Pool[‡]

Delft University of Technology, Delft, Zuid-Holland, 2629 HS, the Netherlands

To meet the required flight simulator-based stall recovery training that will become mandatory for all air-carrier pilots in 2019, many flight simulators will need to be updated with accurate flight models at high angles-of-attack. Using a database of 69 symmetrical and quasi-steady recorded stalls performed with TU Delft's Cessna Citation II laboratory aircraft, this paper aims to show to what extent relevant stall characteristics can still be modeled using flight test data from such "natural" stall flight test data (i.e., without additional flight test inputs). For modeling the (low-frequency) changes to the aerodynamic characteristics, the well-known stall model structure based on Kirchoff's flow separation theory is used. This aerodynamic stall model is augmented with a high-frequency stall buffet model identified based on power spectral density analysis of the flight test linear acceleration data. The stall model identification results obtained from a proposed methodology in which the aerodynamic and buffet model parameters were deliberately jointly estimated shows that the dynamic parameters capturing the stall hysteresis effect can indeed be estimated using quasi-steady stall maneuvers. Aerodynamic terms related to the pitch rate, however, are difficult to estimate for such quasi-steady maneuvers, given the correlation between pitch rate and angle-of-attack. It was found that estimating stall transient effects (i.e., hysteresis time constants), which normally require highly dynamic flight test maneuvers, was found to be improved with with explicit use of the measured accelerations caused by the stall buffet in the identification methodology.

I. Introduction

Aerodynamic stall is a highly dynamic, non-stationary condition where the flow over the wings of the aircraft separates in unpredictable ways, leading to dangerous upset conditions if left uncorrected. Stalls currently are the primary cause of fatal accidents in general aviation, and are an important contributor to fatal accidents in civil aviation.¹⁻³ As a result of new aviation legislation, in 2019 all air-carrier pilots are obliged to go through flight simulator-based stall recovery training.⁴⁻⁶ Until recently simulators were not required to have an accurate representation of flight in the stall regime.⁷⁻⁹ This implies that many aircraft dynamics models driving flight simulators must be updated in the coming years to include accurate stall and post-stall dynamics.

Accurate simulations of high angle-of-attack maneuvers have most often been developed for fighter jets.¹⁰⁻¹² These models were based on wind tunnel data, which included both static and dynamic tests using a rotary balance.¹³ In the current development of stall models for general aviation and large transport jets typically different methods are used. For example, a recent European effort into stall modeling has been performed in the SUPRA project.¹⁴ During this project a stall model for a generic transport aircraft, low-wing configuration and engines positioned under the wings, was created based on wind tunnel and computational fluid dynamics (CFD) data.^{15,16} NASA has pursued the development of a large transport aircraft model for upset conditions, which was created using wind tunnel data and validated with flight data.¹⁷ One issue inherent in wind tunnel modeling, however, are aerodynamic scale effects such as the Reynolds number.⁷ Other efforts have been made in stall modeling, using semi-empirical and analytical data. This included computational methods such as the Vortex Lattice Method (VLM). These methods, however, are primarily used for aircraft design.¹⁸ A similar research has been done in modeling the stall characteristics due to different parts of the aircraft.¹⁹ Current practice is thus that stall models are created using wind tunnel, CFD and

*MSc. student, Control and Simulation Section, Faculty of Aerospace Engineering, P.O. Box 5058, 2600GB Delft, The Netherlands.

[†]Assistant Professor, Control and Simulation Section, Faculty of Aerospace Engineering, P.O. Box 5058, 2600GB Delft, The Netherlands; c.c.devisser@tudelft.nl. Member AIAA.

[‡]Assistant Professor, Control and Simulation Section, Faculty of Aerospace Engineering, P.O. Box 5058, 2600GB Delft, The Netherlands; d.m.pool@tudelft.nl. Member AIAA.

possibly flight data. It has been shown that a wind tunnel based stall model is able to represent stalling dynamics,^{20,21} however, with aerodynamic scale effects that may affect the final flight model.

Currently, when deriving a stall model from flight test data, specifically designed input maneuvers are typically applied for parameter identification.^{22,23} An explicit comparison between quasi-steady stall and dynamic stall data has even been made, showing that the quasi-steady stall models were less robust in explaining flight data.²⁴ It is currently not clear, however, which stall characteristics can perhaps still be modeled based on such quasi-steady stalls. As for instance listed by Gingras et al.,²⁰ the ICATEE committee has proposed several stall characteristics to be modeled, for *representative* stall model simulation, which include: 1) stall buffet, 2) stall hysteresis, 3) changes in pitch stability, 4) degradation in control responses, 5), uncommanded roll response or roll-off, 6) apparent randomness or non-repeatability, and 7) degradation in static/dynamic lateral-directional stability.

In this paper it is investigated to what extent the first two of these characteristics, the stall buffet and the aerodynamic stall hysteresis effects, can still be identified from flight data of quasi-steady symmetrical stall maneuvers, without a side slip measurement. The stall model will be split into a low-frequency and a high-frequency model. The low-frequency model contains the aerodynamic stability and control derivatives, which calculates the baseline for the forces and moments. The high-frequency model adds high-frequency accelerations on top of the accelerations as predicted by the low-frequency model. Essentially, the high-frequency model will be used for re-creating the stall buffet. Both models will be identified from flight test data of a large number of quasi-steady stalls collected with TU Delft's Cessna Citation II laboratory aircraft (PH-LAB).

This paper is structured as follows. First a description of the aircraft will be given, containing information on its mass, inertia, and instrumentation system. Also, an overview of the available flight test datasets will be given in Section II. Secondly the performed flight path reconstruction (FPR) will be explained in Section III. This includes pre-processing of the data, the kinematic equations and algorithm used for FPR, and the post-processing. In Section IV the aerodynamic and buffet model structures are defined, as well as the parameter identification methodology. The results are presented in Section V. The paper ends with a discussion and the main conclusions.

II. Research Vehicle and Flight Data

The aircraft being modeled in this paper is a Cessna Citation II model 550, see Fig. 1. This aircraft, with registration PH-LAB, is property of Delft University of Technology (DUT) and the Netherlands Aerospace Center (NLR). The aircraft is a twinjet business jet, with two Pratt & Whitney JT15D-4 turbofan engines, with a maximum thrust of 11.1 kN each. Its maximum operating speed is 198.6 m/s, with a maximum operating altitude of 13 km.²⁵

II.A. Dimensions and mass properties

The Cessna Citation II is 14.4 meters long and has an outer fuselage diameter of 1.63 meters. The sweep-back of the main wings at 25% chord is 1.4 degrees, and it has a 4.0 deg dihedral. The aircraft basic empty weight (BEW) and inertia properties are given in Table 1. Furthermore the distance between the angle-of-attack vane and the aircraft nose is approximately 4 meters. The attitude and heading reference system (AHRS) is located beneath the floor of the nose baggage compartment, which is the compartment in front of the forward pressure bulkhead, see Fig. 2. The distance between the AHRS system and the nose is approximately 1.9 meters.



Figure 1. TU Delft's Cessna Citation II laboratory aircraft (PH-LAB).

Table 1. Dimensions and mass properties of the aircraft

Dimensions	
b	15.9 m
\bar{c}	2.06 m
S	30.0 m ²
Mass properties	
m	4,157 kg
I_{xx}	12,392 kgm ²
I_{yy}	31,501 kgm ²
I_{zz}	41,908 kgm ²
I_{xz}	2252.2 kgm ²

All values correspond to the basic empty weight.

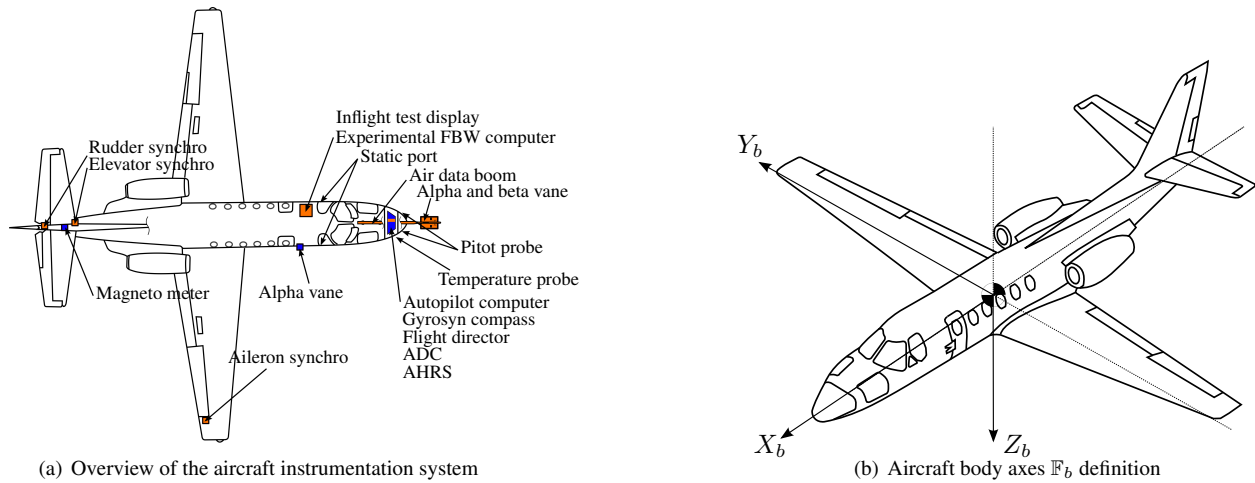


Figure 2. Aircraft instrumentation system and reference frame definition.

II.B. Instrumentation

The PH-LAB laboratory aircraft is equipped with a custom flight test instrumentation system (FTIS), see Fig. 2. The FTIS on the Cessna Citation II contains, among others:

- an AHRS, which contains information on the Euler angles (ϕ, θ, ψ) , the body-axes rotational rates (p, q, r) and the linear accelerations (a_x, a_y, a_z) . The linear accelerations: a_y and a_z were compensated for the gravity component, meaning that in stationary flight these measurements were zero. The linear acceleration in x-direction however did not contain this compensation and thus it measured the specific force. These measurement had a sampling frequency of 50 Hz.
- a digital air data computer (DADC) which measures among others, the true airspeed (V_{TAS}). All measurements by the DADC had a sampling frequency of 16.67 Hz.
- a differential global positioning system (DGPS), which contained information regarding the position and change in position $(\hat{x}, \hat{y}, \hat{h})$. The position was originally measured in longitude, latitude and altitude, but for this research was transformed into flat Earth coordinates (x, y, z) , using a standard transformation matrix. The DGPS measurements had a sampling frequency of 1 Hz.
- an air data boom and an angle-of-attack vane. The air data boom was, however, not available during the data collection for this research project. Therefore only the angle-of-attack vane was used to measure the angle-of-attack (α) , this vane had a sampling frequency of 1000 Hz.
- a set of synchro's on the elevator, aileron, rudder and flaps $(\delta_e, \delta_a, \delta_r, \delta_f)$ to measure the control surface deflections. These were measured with a sampling frequency of 100 Hz.

A summary of the accuracy and update rates of the different sensors is given in Table 2.

II.C. Flight Data

In the third year bachelor course on *Aerospace Flight Dynamics & Simulation* at Delft University of Technology, all students take part in a flight test. During these flight tests, students have to collect flight test data that has to be processed afterwards. Students also experience the eigenmodes of the Cessna Citation II, zero-g flight, and a stall on their flights. These stalls are symmetrical induced and quasi-steady, by slowly approaching the stall speed with approximately 1 kts/s deceleration. In total 69 quasi-steady stalls were used for the development of the stall model, meaning that the pitch rate is approximately zero during the approach to stall. On top of that four stalls were flown using a pull-up maneuver, in which the aircraft pitched up with a load factor of approximately 1.3 g. In each of these dynamically induced stalls were flown in a different configuration: flaps and gear up, flaps at 15° and landing gear up, flaps at 15° and landing gear down and flaps at 40° and landing gear down. In each of these non-cruise configuration two stalls were performed: One quasi-steady stall and a stall with a pull-up maneuver. An overview of

Table 2. Standard update rates and noise standard deviations of the sensors

Variable	Data rate, Hz	Noise σ	Unit	Sensor
x	1	$2.08 \cdot 10^{-1}$	m	GPS
y	1	$2.75 \cdot 10^{-1}$	m	GPS
h	1	$2.29 \cdot 10^{-1}$	m	GPS
\dot{x}	1	n/a	m/s	GPS
\dot{y}	1	n/a	m/s	GPS
\dot{h}	1	$1.08 \cdot 10^{-1}$	m/s	GPS
ϕ	50	$1.62 \cdot 10^{-3}$	rad	AHRS
θ	50	$3.40 \cdot 10^{-4}$	rad	AHRS
ψ	50	$1.13 \cdot 10^{-3}$	rad	AHRS
V_{TAS}	16.67	$8.97 \cdot 10^{-2}$	m/s	DADC
α	1000	$2.10 \cdot 10^{-4}$	rad	alpha-vane
p	50	$9.40 \cdot 10^{-4}$	rad/s	AHRS
q	50	$3.10 \cdot 10^{-4}$	rad/s	AHRS
r	50	$5.90 \cdot 10^{-4}$	rad/s	AHRS
a_x	50	$1.59 \cdot 10^{-2}$	m/s ²	AHRS
a_y	50	$4.74 \cdot 10^{-2}$	m/s ²	AHRS
a_z	50	$8.48 \cdot 10^{-2}$	m/s ²	AHRS
δ_e	100	$1.39 \cdot 10^{-3}$	rad	synchro
δ_a	100	$5.50 \cdot 10^{-4}$	rad	synchro
δ_r	100	$3.90 \cdot 10^{-4}$	rad	synchro

the test maneuvers within the flight envelope is shown in Figure 3. During the stall model development approximately 75% was used for model identification, the other 25% was used for validation. The validation sets are numbered from 1 to 17 in Figure 3.

III. Flight Path Reconstruction

The first step in aerodynamic model identification from flight test data is to perform flight path reconstruction (FPR). This is done to correct certain variables, such as the linear accelerations and the angle-of-attack for instrumentation errors. FPR is essentially state estimation of the aircraft, for which generally a Kalman filter is used. The chosen filter for this research is the Unscented Kalman filter (UKF).^{26,27}

III.A. Pre-processing

As described in Section II, the acquisition rates differ between sensors. One method of coping with this is by using a multi-rate Kalman filter²⁸ (MRKF). For this research, however, FPR can be done offline and thus instead of using a MRKF, the data were re-sampled to a consistent sampling time of 10 ms (100 Hz).

After re-sampling it was necessary to correct the linear acceleration data for an offset with respect to the center of gravity. The linear accelerations are measured by the AHRS system's Inertial Measurement Unit (IMU), which is located approximately 1.9 meters aft of the nose, see Fig. 2. The center of gravity, however, lies between 18.0% and 30.0% of the mean aerodynamic chord (MAC).²⁵ To compensate for this offset the following set of equations can be used:²⁹

$$\begin{aligned}
 a_{x_{cg}} &= a_{x_{ac}} + (x_{cg} - x_{ac}) (q^2 + r^2) - (y_{cg} - y_{ac}) (pq - \dot{r}) - (z_{cg} - z_{ac}) (pr - \dot{q}) \\
 a_{y_{cg}} &= a_{y_{ac}} + (y_{cg} - y_{ac}) (r^2 + p^2) - (z_{cg} - z_{ac}) (qr - \dot{p}) - (x_{cg} - x_{ac}) (qp - \dot{r}) \\
 a_{z_{cg}} &= a_{z_{ac}} + (z_{cg} - z_{ac}) (p^2 + q^2) - (x_{cg} - x_{ac}) (rp - \dot{q}) - (y_{cg} - y_{ac}) (rq - \dot{p})
 \end{aligned} \tag{1}$$

There are two issues in applying Eq.(1) before the FPR. First of all, any biases in the rotational rate data have not been filtered out yet. These biases can be estimated using FPR, by adding explicit bias terms (λ) to the measured acceleration and rotational rates. Assuming that during the maneuver the bias does not change, the time derivative of the bias term ($\dot{\lambda}$) is equal to zero. As shown in Figure 4, however, these biases in rotational rates are, in general, small. Therefore, the error introduced by neglecting the bias in the rotational rates will be small as well. In fact the error caused by not correcting the acceleration measurement for the offset with the center of gravity is larger than assuming that the biases are zero.

Another problem is to obtain the rotational accelerations ($\dot{p}, \dot{q}, \dot{r}$), since these are not measured directly. To obtain these rotational accelerations the rotational rates have to be numerically differentiated. Numerically differentiating the

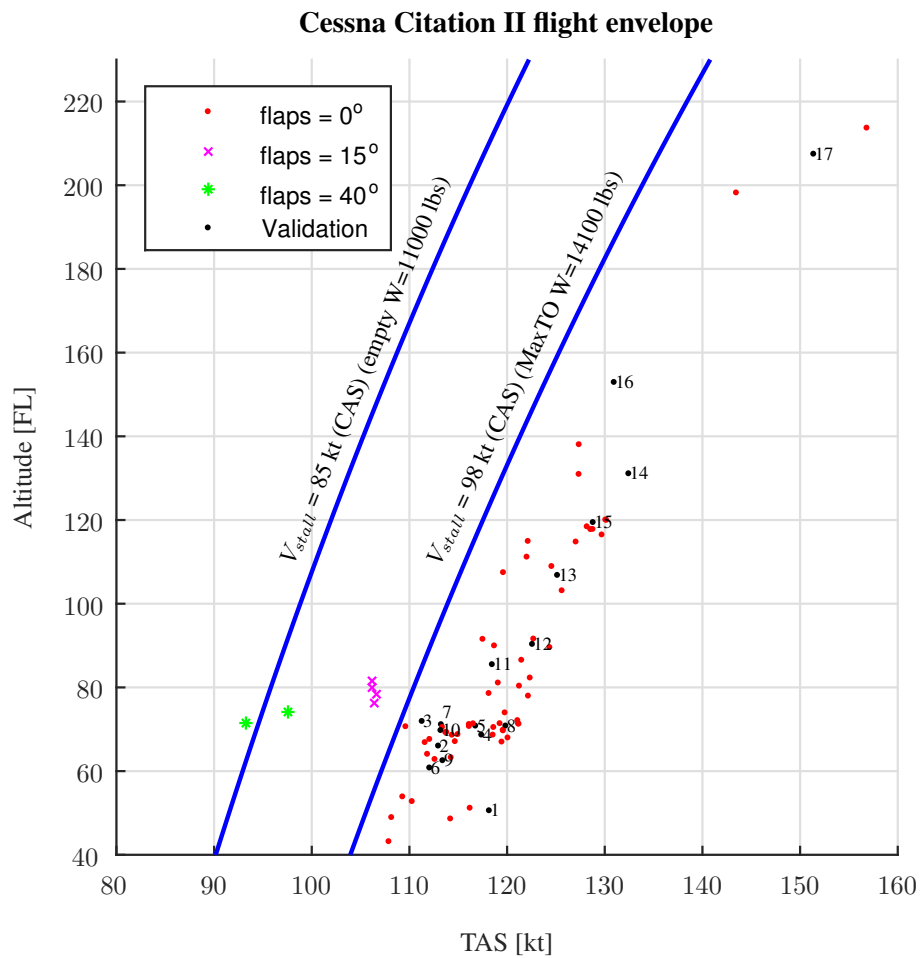


Figure 3. An overview of where the data points were captured within the flight envelope

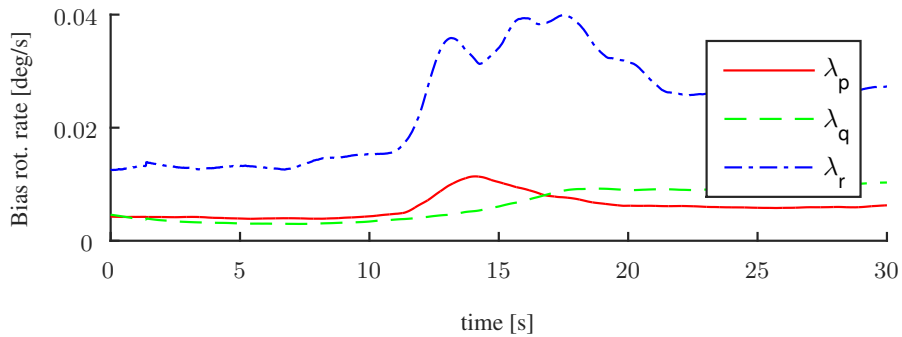


Figure 4. Average bias in the rotational rate measurements.

rotational rates, however, can lead to noise amplification. To prevent this the rotational rates are first filtered, using a zero-phase low-pass filter.³⁰ Then after filtering the rates could be differentiated (still neglecting the bias) to obtain the rotational accelerations.

Furthermore, the center of gravity position needs to be known, this is not a trivial task since the center of gravity changes throughout the flight. To obtain the distance of the center of gravity with respect to the nose, a mass model has been used of the Cessna Citation II.³¹ The BEW was determined by placing the wheels of the aircraft on three separate weight scales. Furthermore the weight of each passenger was measured, as well as the fuel state at the start of the flight. This allowed for accurate estimation of the center of gravity of the aircraft.

Not only do the linear accelerations have to be corrected for the offset in the center of gravity, they also have to be pre-filtered using a low-pass filter. This is due to the stall buffet, which is not captured by the dynamic equations. An example of the raw vertical linear acceleration and the filtered acceleration during a stall is shown in Figure 5. The cut-off frequency was chosen to be 0.8 Hz. The reason for this value is due to the angle-of-attack measurement, which is measured by a physically damped vane. The damping of this vane corresponds to a cut-off frequency of 0.8 Hz, as will be shown in Section III.B.1.

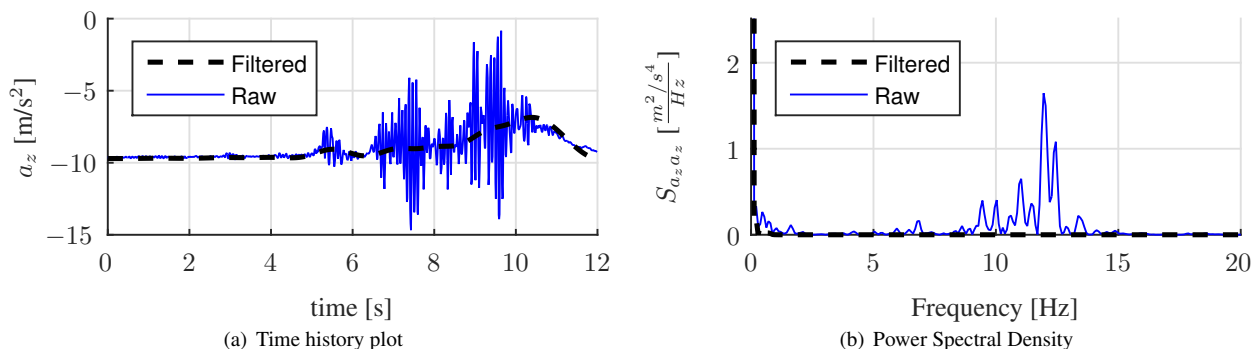


Figure 5. An comparison of the raw and pre-filtered vertical acceleration data.

For the recorded quasi-steady stalls, a measurement of the side slip angle (β) was not available. Without a measurement of the side slip angle the lateral velocity component (v) does not converge well during FPR. Therefore, it is common practice to use a “pseudo-beta” in FPR for longitudinal maneuvers.³² This pseudo-beta is a zero mean white noise signal, for this research the noise intensity was set to 0.01° , which was tuned by trial and error. With the introduction of a pseudo-beta, the estimated values of the side slip angle and the bias term in the lateral acceleration will be meaningless, nonetheless this pseudo-beta improves the performance of the state estimation for longitudinal maneuvers.

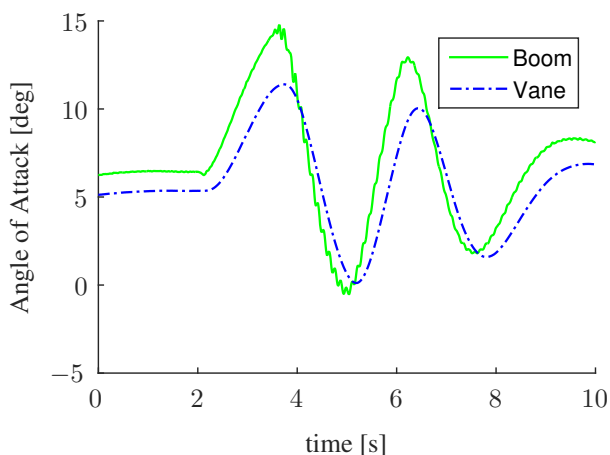


Figure 6. The angle-of-attack as measured by the air data boom and by the angle-of-attack vane.

III.B. Kinematic equations

III.B.1. Alpha-vane dynamics

The aircraft was not equipped with an air-data boom and thus an alpha vane on the fuselage was used to measure the angle-of-attack. This angle-of-attack data is normally not used for model identification because of its inherent mechanical lag ($\tau \approx 0.2$ s). A comparison between a measurement of the air data boom and the alpha-vane is shown in Figure 6. This dataset, in which both the air-data boom and the alpha-vane were available, is from older flight tests performed by Delft University of Technology to collect in-flight pilot control behavior data³³ and flight test data for global nonlinear model identification with multivariate splines.³⁴ From Figure 6 several observations can be made:

1. Body induced velocities are definitely present in the alpha vane, since the angle-of-attack measured by the vane is approximately 1.1 degrees lower than angle-of-attack measured by the boom. Although it must be noted that the boom in this case is the raw signal, and is not corrected for any body induced velocities.
2. The angle-of-attack as measured by the vane is well damped, resulting in a smooth signal. The boom measurements contain higher frequency components.
3. The damping of the vane also causes a lag in its measurement. When comparing the vane with the boom, the vane has a lag of approximately 0.2 seconds. This causes the signal to be low-pass filtered with a cut-off frequency of approximately 5 rad/s (≈ 0.8 Hz).

To capture the effect of the body induced velocities, the angle-of-attack model is extended by: a correction for the pitch rate of the aircraft, a fuselage upwash component on the angle-of-attack ($C_{\alpha_{up}}$) and an unknown wind component in the angle-of-attack (C_{α_0}). The resulting equation is:²⁹

$$\alpha_v^* = (1 + C_{\alpha_{up}}) \arctan \frac{w}{u} - \frac{x_{v\alpha} (q - \lambda_q)}{\sqrt{u^2 + v^2 + w^2}} + C_{\alpha_0} \quad (2)$$

Another issue with the angle-of-attack measured by the vane is the lag of approximately 0.2 seconds. This can be compensated for by modeling the angle-of-attack vane as a first-order filter.³² This filter is given by:

$$\frac{\alpha_v(s)}{\alpha_v^*(s)} = \frac{1}{\tau_v s + 1} \quad \Rightarrow \quad s\alpha_v(s) = \frac{1}{\tau_v} (\alpha_v^*(s) - \alpha_v(s)) \quad (3)$$

Here α_v is the measured angle-of-attack by the vane and α_v^* is the true angle-of-attack in the area of the α -vane, as given in Eq.(2). Combining Eqs. (2) and (3) results in:

$$\dot{\alpha}_v = \frac{1}{\tau_v} (\alpha_v^* - \alpha_v) = \frac{1}{\tau_v} \left[(1 + C_{\alpha_{up}}) \arctan \frac{w}{u} - \frac{x_{v\alpha} (q - \lambda_q)}{\sqrt{u^2 + v^2 + w^2}} + C_{\alpha_0} - \alpha_v \right] \quad (4)$$

where the value of the time constant (τ_v) is set to 0.2 seconds. In practice this time constant could be a function of the flight condition, during this research, however, the time constant was assumed to be constant.

III.B.2. Navigation Equations

The full set of navigation equations, i.e., the kinematic equations of the state, are given by Eq. (5). An important factor in state estimation, however, is that the state should be observable. Observability of the system can be calculated theoretically,³⁵ but this does not necessarily mean that the Kalman filter will converge. Theoretically the system as given by Eq. (5), is fully observable with the observation equations as given in Eq. (6). It was observed that the vertical wind component (W_{z_E}) would not converge. Furthermore the variables $C_{\alpha_{up}}$ and C_{α_0} are considerably correlated, as shown in Figure 7. This correlation can also be seen in Figure 8, where until the stall, both $C_{\alpha_{up}}$ and C_{α_0} could not converge. Therefore the unknown wind component (C_{α_0}) was removed from the state equations. The effect on the reconstructed angle-of-attack is shown in Figure 7, as can be seen there is no clear difference between using both $C_{\alpha_{up}}$ and C_{α_0} or only using $C_{\alpha_{up}}$.

$$\begin{aligned}
\dot{x} &= [u \cos \theta + (v \sin \phi + w \cos \phi) \sin \theta] \cos \psi - (v \cos \phi - w \sin \phi) \sin \psi + W_{x_E} \\
\dot{y} &= [u \cos \theta + (v \sin \phi + w \cos \phi) \sin \theta] \sin \psi + (v \cos \phi - w \sin \phi) \cos \psi + W_{y_E} \\
\dot{z} &= -u \sin \theta + (v \sin \phi + w \cos \phi) \cos \theta \\
\dot{u} &= (a_x - \lambda_x) - g \sin \theta - (q - \lambda_q) w + (r - \lambda_r) v \\
\dot{v} &= (a_y - \lambda_y) - (r - \lambda_r) u + (p - \lambda_p) w \\
\dot{w} &= (a_z - \lambda_z) - (p - \lambda_p) v + (q - \lambda_q) u \\
\dot{p} &= (p - \lambda_p) + (q - \lambda_q) \sin \phi \tan \theta + (r - \lambda_r) \cos \phi \tan \theta \\
\dot{q} &= (q - \lambda_q) \cos \phi - (r - \lambda_r) \sin \phi \\
\dot{r} &= (q - \lambda_q) \frac{\sin \phi}{\cos \theta} + (r - \lambda_r) \frac{\cos \phi}{\cos \theta} \\
\dot{W}_{x_e} &= 0.01 w_r \\
\dot{W}_{y_e} &= 0.01 w_r \\
\dot{C}_{\alpha_{up}} &= \frac{0.1\pi}{180} w_r \\
\dot{\lambda}_x &= 0 \\
\dot{\lambda}_y &= 0 \\
\dot{\lambda}_z &= 0 \\
\dot{\lambda}_p &= 0 \\
\dot{\lambda}_q &= 0 \\
\dot{\lambda}_r &= 0 \\
\dot{\alpha}_v &= \frac{1}{\tau_v} \left((1 + C_{\alpha_{up}}) \arctan \frac{w}{u} - \frac{x_{v\alpha} (q - \lambda_q)}{\sqrt{u^2 + v^2 + w^2}} - \alpha_v \right)
\end{aligned} \tag{5}$$

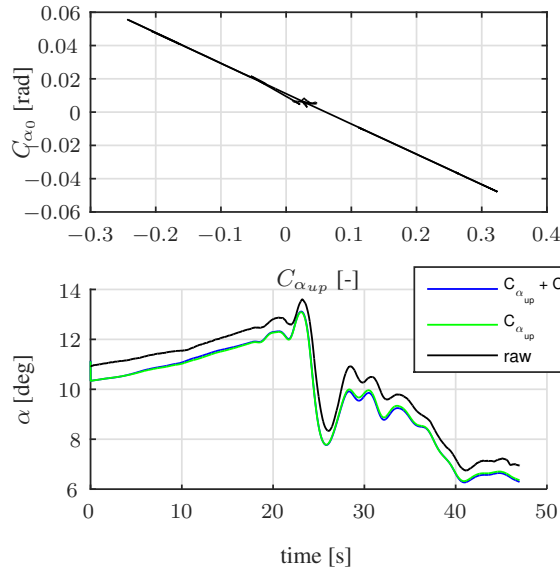


Figure 7. Top: Correlation between $C_{\alpha_{up}}$ and C_{α_0} . Bottom: Difference on the estimated angle-of-attack.

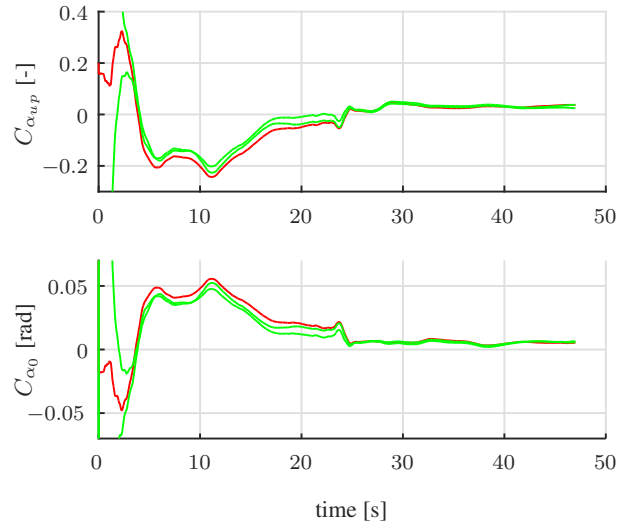


Figure 8. Upwash coefficient $C_{\alpha_{up}}$ and unknown wind component C_{α_0} for three different initial conditions.

The other variable, the vertical wind component (W_{z_E}) had to be omitted as well. Most flight tests, however, were done in relatively calm weather, in which the vertical wind components are in the order of 0.1 to 0.2 m/s.³⁶ Therefore, this omission introduces a small but unpreventable error in the FPR.

Furthermore, it is assumed that bias in the linear accelerations and rotational rates is constant throughout the maneuver. The wind components in the horizontal plane and the up wash coefficient, however, might not be constant throughout the stall maneuver. Therefore, these time derivatives are modeled as a random walk, to give the Kalman filter more freedom in changing these values.

Lastly the gravity components in the equations for \dot{v} and \dot{w} are omitted, due to the correction of these measurements for the gravity components, as explained in Section III.A.

III.B.3. Observation Equations

The observation equations of the FPR model are given in Eq. (6). The DGPS was used to obtain the position and velocity in the Earth Centered Earth Fixed (ECEF) frame. The DADC was used for the true airspeed. The AHRS was used for the Euler angles and the alpha-vane was used to obtain the angle-of-attack. The value of the side slip angle was unavailable and therefore a pseudo-beta is used, as was explained in Section III.A.

$$\begin{aligned}
x_{gps} &= x \\
y_{gps} &= y \\
h_{gps} &= -z \\
\dot{x}_{gps} &= [u \cos \theta + (v \sin \phi + w \cos \phi) \sin \theta] \cos \psi - (v \cos \phi - w \sin \phi) \sin \psi + W_{x_E} \\
\dot{y}_{gps} &= [u \cos \theta + (v \sin \phi + w \cos \phi) \sin \theta] \sin \psi + (v \cos \phi - w \sin \phi) \cos \psi + W_{y_E} \\
\dot{h}_{gps} &= u \sin \theta - (v \sin \phi + w \cos \phi) \cos \theta \\
\phi_{AHRS} &= \phi \\
\theta_{AHRS} &= \theta \\
\psi_{AHRS} &= \psi \\
V_{TAS} &= \sqrt{u^2 + v^2 + w^2} \\
\alpha_{vane} &= \alpha_v \\
\beta_{pseudo} &= \arctan \left(\frac{v}{\sqrt{u^2 + w^2}} \right)
\end{aligned} \tag{6}$$

III.C. Post-processing

After the state estimation, it is necessary to add the gravity acceleration components in y- and z-directions, to the measured accelerations by the AHRS. This can be done by a ECEF frame to body frame transformation, where gravity is defined negative downward. The transformation matrix from the ECEF to the body frame is given by:

$$\mathbb{T}_{bE} = \begin{bmatrix} \cos(\theta) \cos(\psi) & \cos(\theta) \sin(\psi) & -\sin(\theta) \\ \sin(\phi) \sin(\theta) \cos(\psi) - \cos(\phi) \sin(\psi) & \sin(\phi) \sin(\theta) \sin(\psi) + \cos(\phi) \cos(\psi) & \sin(\phi) \cos(\theta) \\ \cos(\phi) \sin(\theta) \cos(\psi) + \sin(\phi) \sin(\psi) & \cos(\phi) \sin(\theta) \sin(\psi) - \sin(\phi) \cos(\psi) & \cos(\phi) \cos(\theta) \end{bmatrix} \tag{7}$$

Lastly the thrust has to be calculated for the model identification. This thrust is calculated using a look-up table of the Pratt & Whitney JT15D-4 turbofan engine, with as inputs the fan speed ($N1$) and the Mach number.

IV. Aerodynamic Model Identification

The stall model identified in this paper is divided into two sub-models: 1) a low-frequency aerodynamic model and 2) a high-frequency stall buffet model. The aerodynamic model will calculate all the aerodynamic forces and moments on the aircraft. This model is based on well-known aerodynamic stability and control derivatives, such as $C_{m_{\delta_e}}$.³⁷ The lift, drag, and pitch moment equations, however, are augmented using Kirchhoff's theory of flow separation.^{24,38} The lateral model is created by modeling the forces for each wing separately. The buffet model adds high-frequency periodic components on top of the baseline accelerations, to reproduce the vibrations due to the flow separation.

IV.A. Aerodynamic Model

The low-frequency aerodynamic model is based on Kirchhoff's theory of flow separation, which has been applied before to a large transport aircraft³⁸ and turboprop aircraft.²⁴ Kirchoff's theory directly links the attainable lift coefficient to the flow separation point on the wing. This can be modeled using Eq. (8), where X is the flow separation point. When the flow is fully attached the flow separation point (X) has a value of one, whereas a fully detached flow gives a value of zero.

$$C_L(\alpha, X) = C_{L_\alpha} \left\{ \frac{1 + \sqrt{X}}{2} \right\}^2 \alpha \tag{8}$$

The flow separation point is modeled as a differential equation:³⁸

$$\tau_1 \frac{dX}{dt} + X = \frac{1}{2} \{1 - \tanh(a_1 (\alpha - \tau_2 \dot{\alpha} - \alpha^*))\} \quad (9)$$

As can be seen in Eq. (9), the flow separation point is a function of the angle-of-attack and the angle-of-attack rate. In total there are four parameters that can be used for “tuning” this function. The parameters a_1 and α^* influence the steady conditions of the stall model, i.e., $\dot{\alpha} = 0$. The values of τ_1 and τ_2 relate to the dynamic effects of the stall, i.e., $\dot{\alpha} \neq 0$. An overview of the effects each parameter has, is given below:

- a_1 : Influences the abruptness of the stall. A low value of a_1 indicates that the stall is not very abrupt, while a high value does the opposite.
- α^* : The angle-of-attack at which the flow separation point equals a half. An increase in α^* indicates a higher critical angle-of-attack.
- τ_1 : Influences the transient effects of the flow separation point, it is essentially a time delay in the flow separation point. A high value indicates a large time delay.
- τ_2 : Determines the hysteresis effect, a higher value indicates that flow separation occurs later with a positive angle-of-attack rate ($\dot{\alpha}$).

Visualizations of these different parameters on the $C_L - \alpha$ curve are given in Figures 9, 10, 11 and 12. In Figures 9 and 10 the flow separation point is described as X_0 , as shown on the y-axis in the right figures. This indicates a steady flow separation point, i.e. $\dot{\alpha} = 0$. Most of the flown stalls are quasi-steady, and thus during approach to stall $\dot{\alpha} \approx 0$. This makes it rather difficult to estimate τ_1 . In fact, estimating the value of τ_1 is not possible using only quasi-steady stall maneuvers, without correlation with other parameters.³⁸

IV.A.1. Longitudinal Aerodynamic Model

The low-frequency longitudinal forces and moment are modeled using Eqs.(10), (11) and (12). The damping terms, i.e., terms related to the pitch rate were omitted from the equations. As will be shown in Section V, the identification of C_{L_q} is feasible, but the parameters C_{D_q} and C_{m_q} , however, are not identifiable.

$$C_L = C_{L_0} + C_{L_\alpha} \left\{ \frac{1 + \sqrt{X}}{2} \right\}^2 \alpha \quad (10)$$

$$C_D = C_{D_0} + C_{D_\alpha} \alpha + C_{D_X} (1 - X) \quad (11)$$

$$C_m = C_{m_0} + C_{m_\alpha} \alpha + C_{m_{\delta_e}} \delta_e + C_{m_X} (1 - X) \quad (12)$$

IV.A.2. Lateral Aerodynamic Model

Due to the unavailability of the side slip measurement, an alternate model structure is used for modeling lateral effects during stall.³⁹ This is done by calculating the lift and drag for both wings separately. The difference in lift and drag causes a rolling and yawing moment, which can be modeled using Eqs. (13) and (14), where Δy is the effective lever arm. The control effectiveness, i.e., $C_{l_{\delta_a}}$ and $C_{n_{\delta_r}}$, could be extracted from the original flight model, with a possible reduction to model the reduced control effectiveness.

$$C_l = (C_{Z_{\text{right}}} - C_{Z_{\text{left}}}) \Delta y \quad (13)$$

$$C_n = (C_{X_{\text{left}}} - C_{X_{\text{right}}}) \Delta y \quad (14)$$

To calculate the lift for both wings separately a distinction can be made between the angle-of-attack experienced by both wings. Effects such as the side slip angle, roll rate and yaw rate all have effect on the local angle-of-attack on the aircraft. The following distinctions are made between these effects:

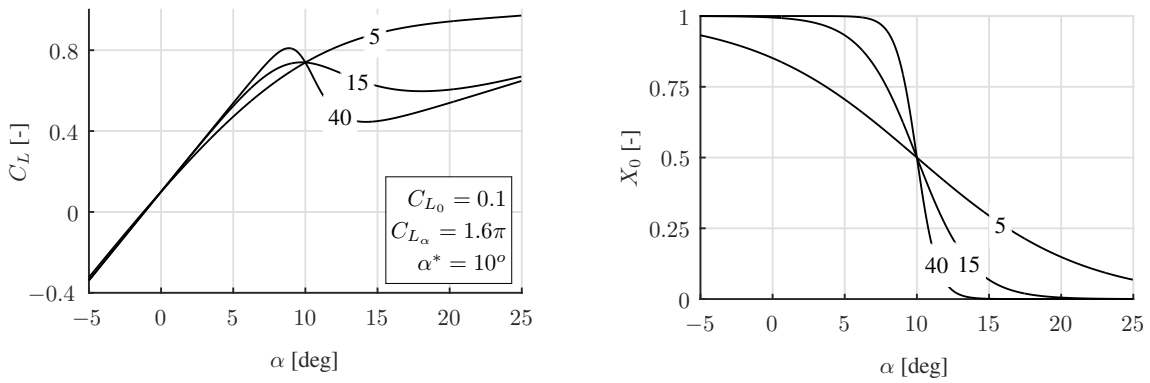


Figure 9. Effect of a_1 on the lift coefficient and flow separation point in steady conditions, adapted from Refs. 24 and 38.

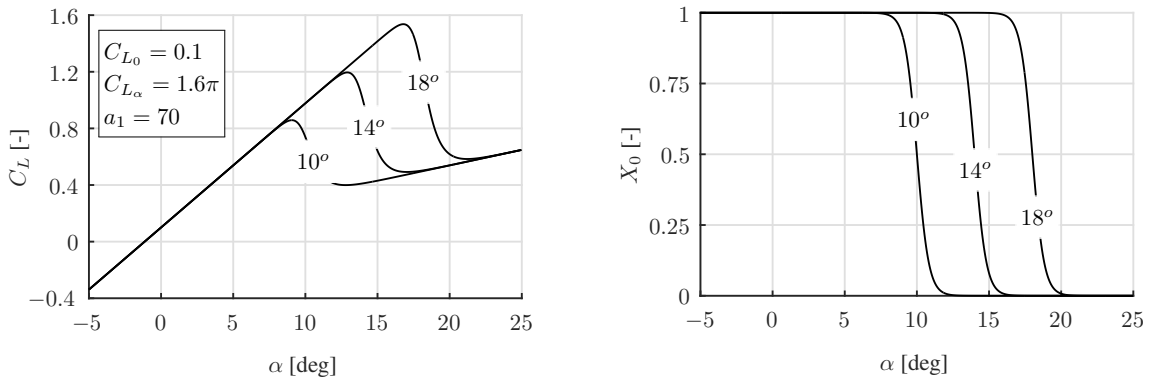


Figure 10. Effect of α^* on the lift coefficient and flow separation point in steady conditions, adapted from Refs. 24 and 38.

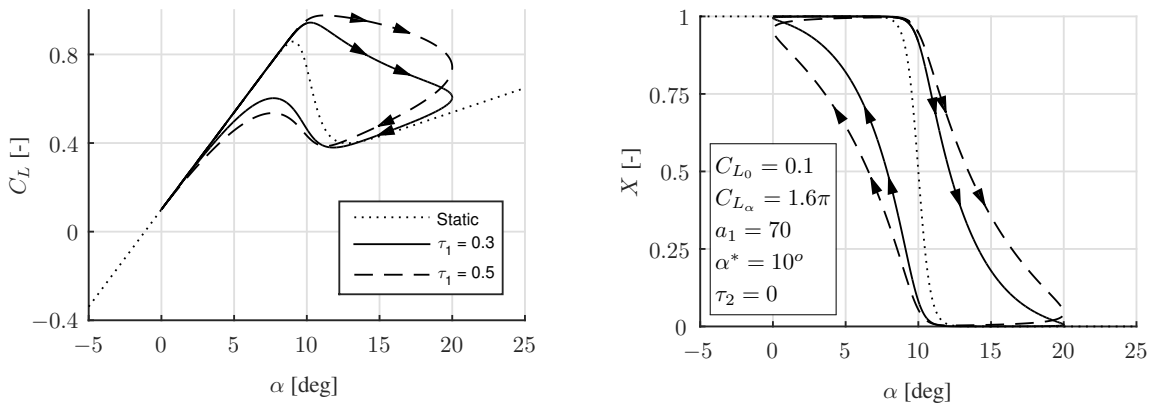


Figure 11. Effect of τ_1 on the lift coefficient and flow separation point in steady conditions, adapted from Refs. 24 and 38.

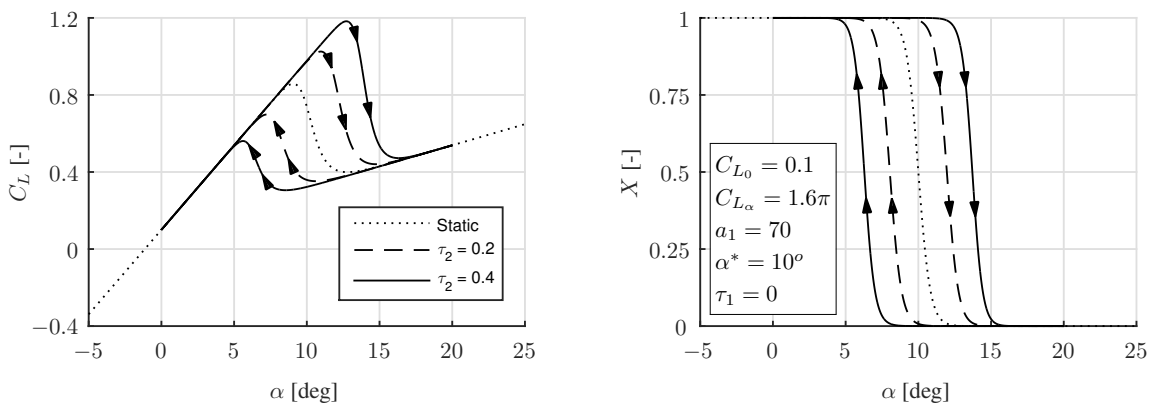


Figure 12. Effect of τ_2 on the lift coefficient and flow separation point in steady conditions, adapted from Refs. 24 and 38.

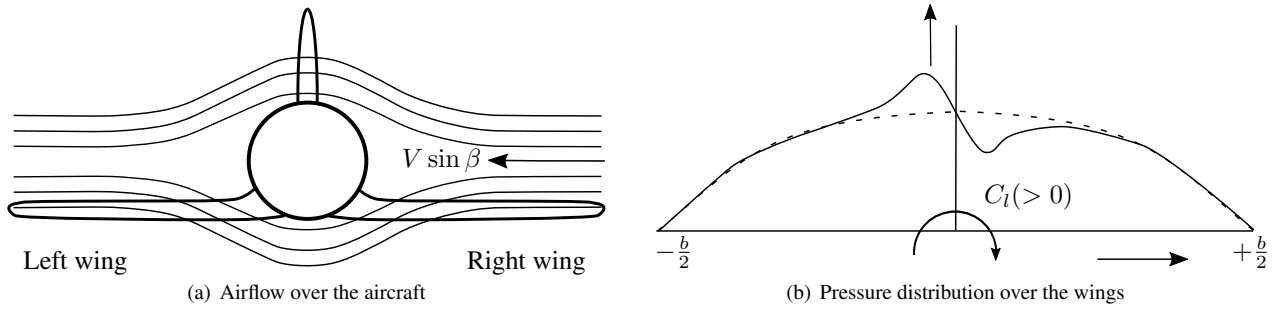


Figure 13. Rolling moment caused by wing-fuselage interaction in side slipping flight, adapted from Ref. 40.

1. **Angle of side slip:** For an aircraft with a low wing configuration a positive side slip angle will decrease the angle-of-attack on the forward wing and increase the angle-of-attack on the backward wing.⁴⁰ This effect is caused by the wing-fuselage interaction, as shown in Figure 13. Although this interaction does have an effect on the local angle-of-attack it is difficult to model, especially without a side slip measurement.

Another effect is caused by the wing dihedral.⁴⁰ Assuming that the aircraft has a side slip from the right, as shown in in Figure 14, it can be seen that the normal velocity on the wings can be calculated as follows:

$$V_{n_l} = w \cos \Lambda - v \sin \Lambda \quad \text{and} \quad V_{n_r} = w \cos \Lambda + v \sin \Lambda \quad (15)$$

The local angle-of-attack can then be calculated using Eq. (16), following from Figure 14:

$$\alpha_{w_l} = \arctan \left(\frac{V_{n_l}}{u} \right) \quad \text{and} \quad \alpha_{w_r} = \arctan \left(\frac{V_{n_r}}{u} \right) \quad (16)$$

So with a positive dihedral and a positive side slip, the right wing will experience a higher local angle-of-attack than the left wing.

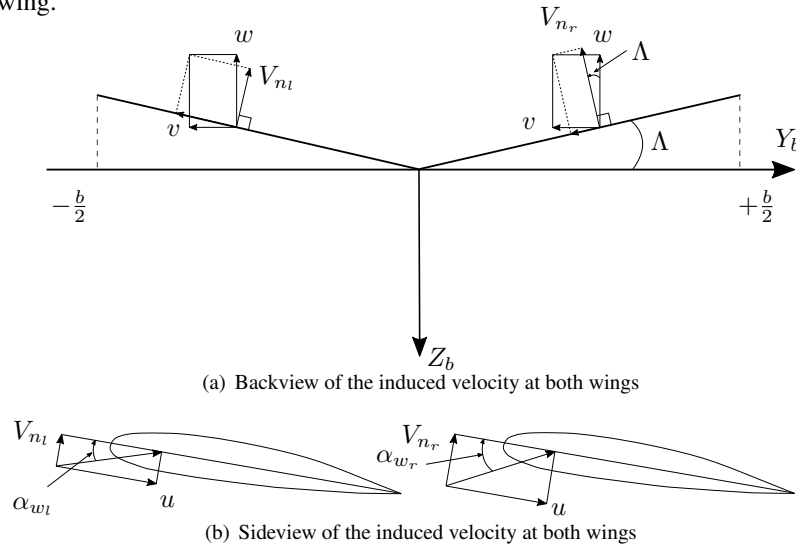


Figure 14. Effect of side slip on an aircraft with wing dihedral, adapted from Ref. 40.

2. **Roll rate:** When the aircraft is rolling, the down going-wing experiences a higher angle-of-attack than the up-going wing. Normally this would damp the rolling motion of the aircraft, but at attitudes near the critical angle-of-attack, the down-going wing could stall while the up-going wing does not. This phenomena is called auto rotation. The change in the angle-of-attack can be calculated using Eq. (17), where y is the position at the wing:⁴⁰

$$\Delta \alpha_{w_l} = -\frac{pb}{2V} \frac{y - y_{c.g.}}{b/2} \quad \text{and} \quad \Delta \alpha_{w_r} = \frac{pb}{2V} \frac{y - y_{c.g.}}{b/2} \quad (17)$$

3. **Yaw rate:** A yawing moment also causes a difference in force generated by the two wings. This is caused by the rotation in which the outer board wing locally experiences a higher velocity than the inboard wing. The local velocity on the wing changes as follows:⁴⁰

$$\frac{\Delta V_l}{V} = \frac{rb}{2V} \frac{y}{b/2} \quad \text{and} \quad \frac{\Delta V_r}{V} = -\frac{rb}{2V} \frac{y}{b/2} \quad (18)$$

IV.B. Buffet Model

The other model that was obtained from the flight data is the high-frequency buffet model. When the flow starts separating from the wing, a vibration can be felt throughout the aircraft. This vibration was measured by the AHRS, which was used for developing a buffet model. The time signal of the vibration was transformed to the frequency spectra, to obtain the power spectral density (PSD) for each stall. To obtain a more accurate results these power spectral densities were averaged to obtain one periodogram. Before doing so, however, it was first investigated whether altitude had a significant effect on the PSD. As shown in Figure 15, there seems to be no clear effect of altitude on the stall buffet in the collected stall data. Therefore, one stall buffet for all altitudes will be modeled in this paper.

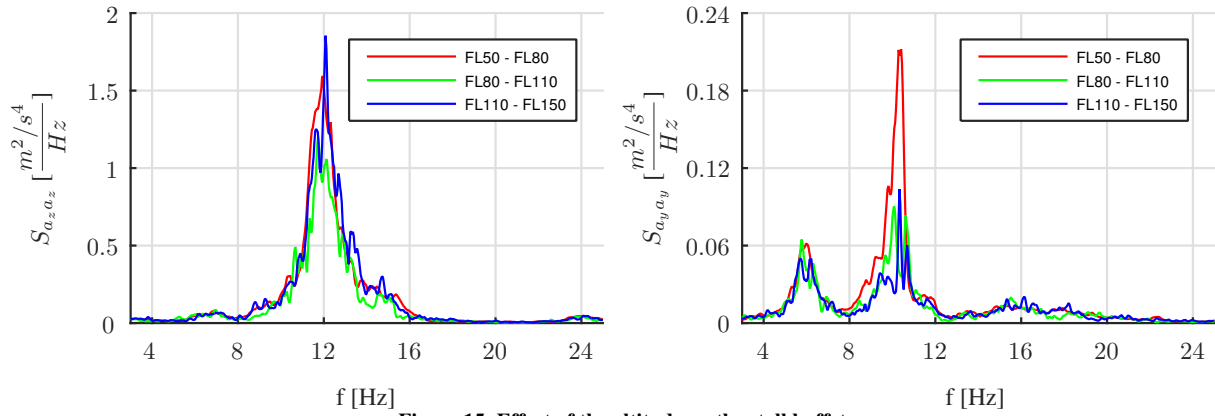


Figure 15. Effect of the altitude on the stall buffet.

As shown in Figure 15, the PSD of the vertical acceleration (a_z) is approximately ten times larger than the lateral acceleration (a_y). This indicates that the vertical acceleration is the most dominant. The reason for not showing the PSD for the acceleration in x-direction is that this signal is effectively zero. Furthermore it can also be seen already in Figure 15 that the vertical buffet has one dominant frequency, around 12 Hz. The lateral buffet has two dominant frequencies: one at 6 Hz and one at 10 Hz

The buffet model is assumed to be a white noise signal, which is passed through a shaping filter. This model structure is shown in Eq. (19). The stall buffet frequency response function ($H(j\omega)$) can be estimated from the PSD as shown in Figure 15, assuming that the driving white noise input signal u has an intensity of one.

$$S_{yy} = |H(j\omega)|^2 S_{uu} \quad (19)$$

The stall buffet models are created using a second-order filter, as given in Eq. (20). The resonance frequency of a second-order filter can be used to create a bandpass filter. For the vertical buffet model one bandpass filter is used, whereas for the lateral buffet model two bandpass filters were added together, as shown in Figure 16.

$$H(j\omega) = \frac{H_0 w_0^2}{(j\omega)^2 + \frac{w_0}{Q_0} j\omega + w_0^2} \quad (20)$$

IV.C. Parameter Estimation

Both the aerodynamic model and the buffet model are nonlinear functions, and thus estimating their parameters becomes a nonlinear optimization problem. The solver that was used, is based on a trust-region-reflective optimization algorithm.⁴¹ One of the major problems associated with nonlinear optimization, is that a final value could be a local optimum. To increase the chance of finding the global optimum two techniques were applied simultaneously:

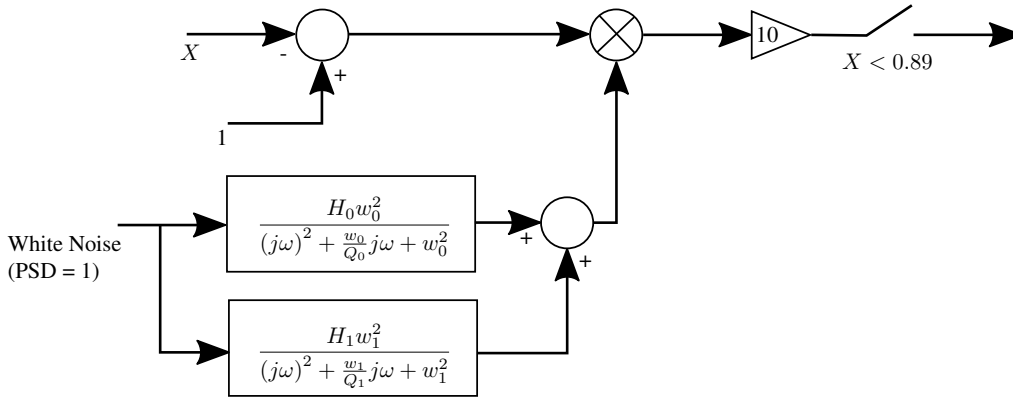


Figure 16. Lateral stall buffet model including the effect of the flow separation point.

1. The estimated parameters were constrained when possible. For example it is known that: $C_{D_0} > 0$, otherwise the aircraft would be a perpetual motion machine. Another constraint is that $C_{L_\alpha} > 0$. Using such constraints the optimization problem becomes bounded and it is more likely that a global optimum will be found.
2. The optimization algorithm was run for multiple sets of initial conditions. A nonlinear optimization problem always needs a set of initial conditions, these conditions influence the possibility of finding the global optimum. When a large set of initial conditions is used, the solution with the lowest mean squared error can be chosen to be the best estimate. The set of initial conditions was chosen by first running a large set of randomly picked initial conditions through the cost function. Then a certain amount, e.g., 500, initial conditions were chosen from the larger set. This is done by obtaining the 500 initial conditions, which gave the lowest value for the cost function.

Since most stalls were quasi-steady they could not be used for estimating the transient effects (τ_1). Another method for estimating the value of τ_1 was found instead. To do so first all parameters, including the hysteresis constant (τ_2) were estimated using a nonlinear least squares approach.⁴² During this estimation the value of τ_1 was kept fixed. The cost function that was used is given in Eq. (21), with X being defined as in Eq. (9). The constraints are as given in Table 3, as well as the initial conditions. The initial conditions were chosen as a base value plus a random number selected from the standard normal distribution, with a standard deviation of σ .

$$\begin{aligned}
 J = & \left(C_{L_0} + C_{L_\alpha} \left\{ \frac{1+\sqrt{X}}{2} \right\}^2 \alpha - C_L \right)^2 \\
 & + (C_{D_0} + C_{D_\alpha} \alpha + C_{D_X} (1 - X) - C_D)^2 \\
 & + (C_{m_0} + C_{m_\alpha} \alpha + C_{m_{\delta_e}} \delta_e + C_{m_X} (1 - X) - C_m)^2
 \end{aligned} \tag{21}$$

Table 3. Constraints and initial conditions for the optimization algorithm

Parameter	C_{L_0}	C_{L_α}	a_1	α^* [rad]	τ_2 [s]	C_{D_0}	C_{D_α}	C_{D_X}	C_{m_0}	C_{m_α}	$C_{m_{\delta_e}}$	C_{m_X}
Lower-bound	-2	0	0	0	0	0	0	0	-2	-2	-2	-2
Upper-bound	2	2π	120	0.5	2	2	2	2	2	0	0	0
Initial condition	0.5	3.0	50	0.2	0.25	0.1	0.5	0.4	0.0	-0.5	-0.3	-0.2
σ	0.5	2.0	50	0.2	0.25	0.1	0.5	0.4	0.2	0.5	0.3	0.2

Figure 17 provides a graphical representation of the parameter estimation workflow. As is clear from Figure 17, the estimation of the aerodynamic and flow separation parameters was performed in two steps. When these parameters as shown in Figure 17 were optimized they were used in the stall buffet model.

The buffet is driven by a white noise signal, with a PSD equal to one. This signal is then shaped by a bandpass filter, corresponding to the stall buffet. To increase the amplitude of the stall buffet as a function of the flow separation point, the buffet signal will be multiplied with $(1 - X)$, where X is determined using Eq. (9). This, however, decreases the amplitude of the original signal, which can be corrected for using a gain. This gain can later on also be used for tuning the amplitude, such that the accelerations are in within limits of a full motion simulator. Finally the stall buffet will have a certain threshold before the signal is activated, e.g., the buffet will only be felt in case $X < 0.89$. A schematic overview of this buffet signal generator is given in Figure 16.

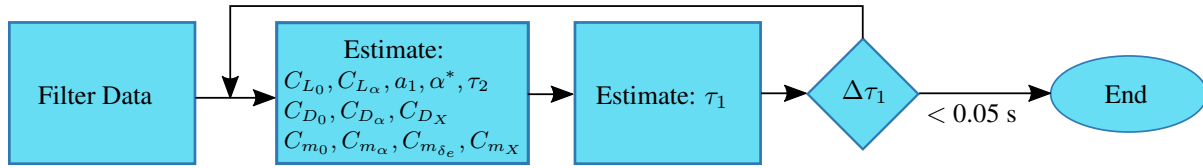


Figure 17. Aerodynamic and flow separation model parameter estimation workflow.

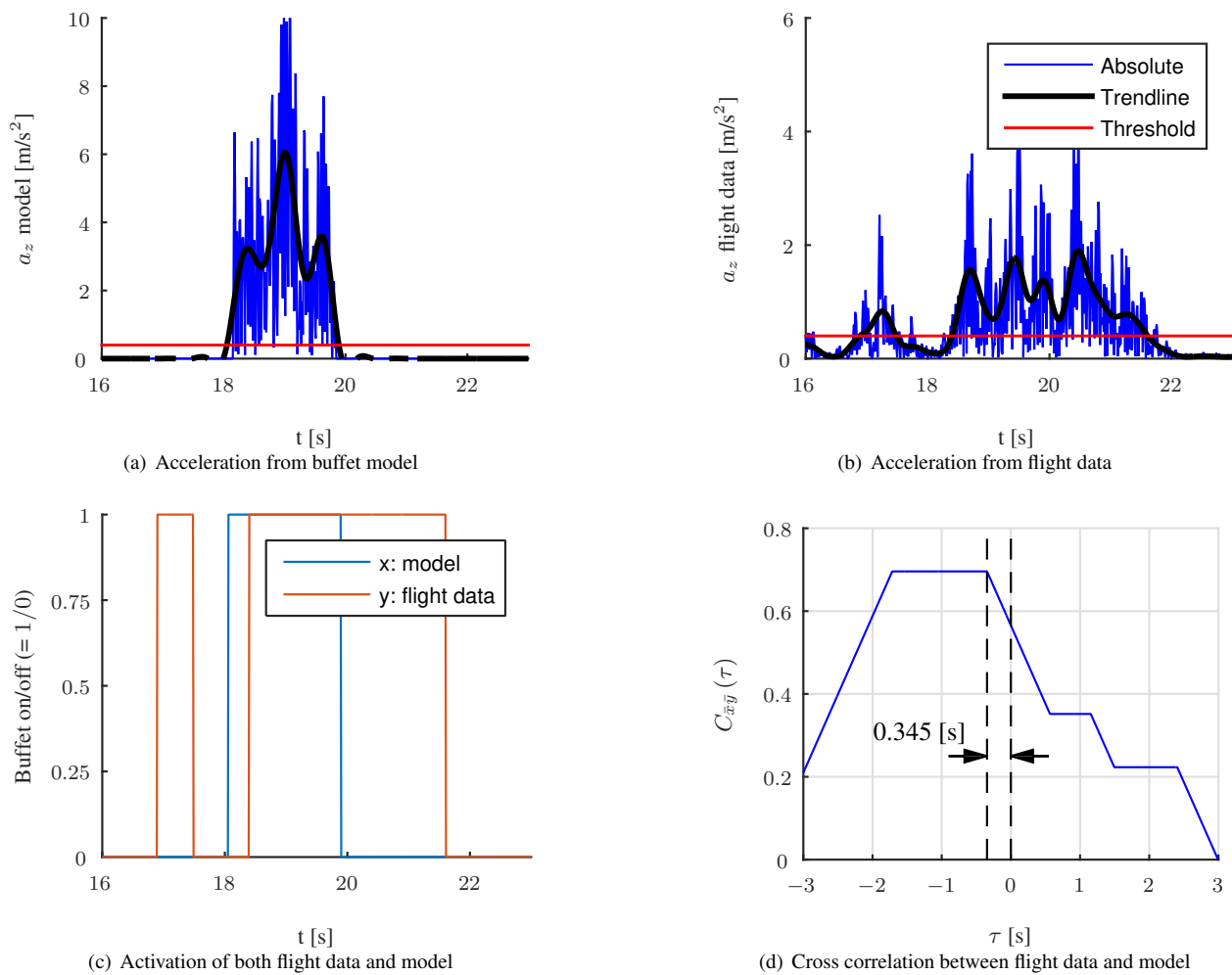


Figure 18. Graphical overview of the steps being taken to estimate τ_1 .

During the validation of the stall buffet it was found that, most of the time, the vibration of the model stopped earlier than from the flight data. This difference indicated that a transient effect was not taken into account in the stall model buffet. This transient effect is essentially the value of τ_1 and thus this allows for estimating τ_1 based on the buffet acceleration data.

To do so an algorithm was made to detect when the stall buffet was active. First the acceleration was filtered by a high-pass filter. Then the absolute value of the high-pass filtered acceleration is taken, shown as the blue line in Figure 18a. This signal is then low-pass filtered to obtain a general trend of the stall buffet, as shown by the black line in Figure 18a. This trend was then compared to a certain threshold (red line in Figure 18a), in this case 0.4 m/s^2 . When the low-pass filtered absolute acceleration data (black line) got above the threshold (red line), the buffet was said to be active, otherwise the buffet was non-active. The same method was applied for the acceleration data obtained by an initial stall buffet model, as shown in Figure 18b. The activate and non-active sections from both the flight data and the stall model are compared, as shown in Figure 18c. The first trigger (i.e., from non-active to active) was used to obtain the onset flow separation point. This was done by calculating the stall model buffet for a set of thresholds. Then the threshold which matched the first triggers of both the model and the flight data the closest, was chosen as the best threshold.

The lag, i.e., τ_1 , was estimated by calculating the cross correlation of the both the “active/ non-active” signal (as shown in Figure 18c). The estimated delay was given by the negative of the lag, for which the cross-correlation has the largest absolute value. In case more than one lag was found for the largest absolute value of the cross-correlation, the delay was chosen to be the smallest (in absolute value) of these lags, an example of this is given in Figure 18d, where the time delay was found to be 0.345 s. This was done for all model identification data sets, for a large set of random seeds for the white noise signal, which drives the stall buffet model.

Initially the stall parameters, however, were estimated with the assumption that τ_1 was zero. To obtain a better estimate the optimization algorithm, which obtains all parameters except for τ_1 , was run again. This time however with the value of τ_1 as found from the stall buffet analysis. After doing so these parameters were used again to re-estimate τ_1 . This process is iterated, until the change in τ_1 is sufficiently small. This iterative process is also shown in Figure 17. As shown by Eqs. (10), (11) and (12), the dependent variables are the longitudinal force, vertical force and the pitch moment. These values cannot be measured directly and thus have to be calculated from the aircraft equations of motion:

$$C_X = \frac{ma_x}{\frac{1}{2}\rho V_{TAS}^2 S} - \frac{T}{\frac{1}{2}\rho V_{TAS}^2 S} \quad (22)$$

$$C_Z = \frac{ma_z}{\frac{1}{2}\rho V_{TAS}^2 S} \quad (23)$$

$$C_m = \frac{1}{\frac{1}{2}\rho V_{TAS}^2 S \bar{c}} (I_{yy}\dot{q} - (I_{zz} - I_{xx})rp - I_{xz}(r^2 - p^2)) \quad (24)$$

From Eqs. (22) and (23), the lift and drag forces can be calculated, using the standard transformation from body to aerodynamic frame, assuming zero side slip:

$$C_L = -C_Z \cos(\alpha) + C_X \sin(\alpha) \quad (25)$$

$$C_D = -C_Z \sin(\alpha) - C_X \cos(\alpha) \quad (26)$$

Lastly the moment equation has to be corrected for the moment caused by the engine. The engine is located above the center of gravity, this distance (Δz) is on average approximately 0.5 meters. This moment caused by the engine causes an extra nose down moment and thus the moment induced by the engine has to be added to the moment as calculated by Eq. (24), which is done as follows:

$$C_{m_{corr}} = C_m + \frac{T\Delta z}{\frac{1}{2}\rho V_{TAS}^2 S \bar{c}} \quad (27)$$

V. Results

V.A. Flight Path Reconstruction

An example of the state estimation results is given in Figures 19 and 20. The former shows the raw and reconstructed measurements. It can be noticed that the alpha-vane model seems to work correctly, since the signal is shifted approximately 0.2 seconds back in time. Another interesting note is that of the pseudo-beta. During the stall the aircraft has a small bank angle, which most likely causes a small side slip angle. As can be seen in Figure 19, the input data for the side slip angle is zero, whereas the reconstructed value is not.

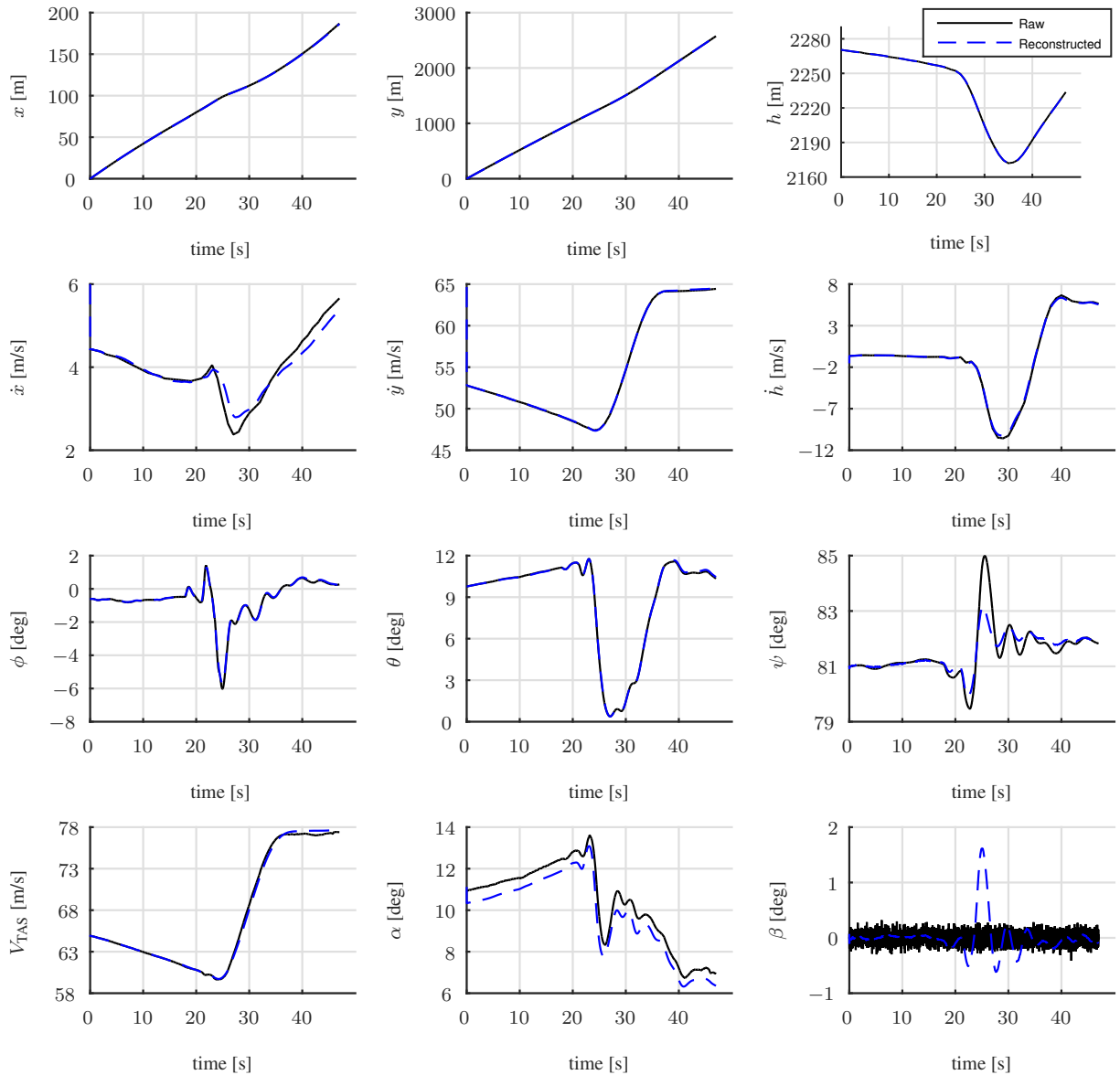


Figure 19. Example of FPR results for a stall occurring at $t = 23$ s.

In Figure 20 the estimate of the states, which are not directly measured, can be seen. A simple check for convergence is to run the Kalman filter for different initial conditions. When these signals still converge to one value it can be assumed that the state reconstruction is indeed converging. An example of this was shown in Figure 8. It is not shown, however, in Figure 20 since all lines coincided within a second. Furthermore it can be seen that the fuselage upwash component on the angle-of-attack measurement ($C_{\alpha_{up}}$) is not zero. This indicates that body induced velocities are definitely present at the alpha-vane.

The bias terms and the wind terms on the other hand seem to be varying a little. It must be noticed, however, that these terms most likely do not only contain the pure biases, but other effects as well. These effects could for example be: a small misalignment in the IMU, an error in correcting the linear accelerations for the center of gravity and a high value of dilution of precision (DOP) in the GPS system.

Another interesting effect is the bias term in the yaw rate (λ_r), which seems to be rather high and also changes during the stall maneuver. A logical explanation seems to be that there is not enough excitation in yaw direct, making it difficult to identify.

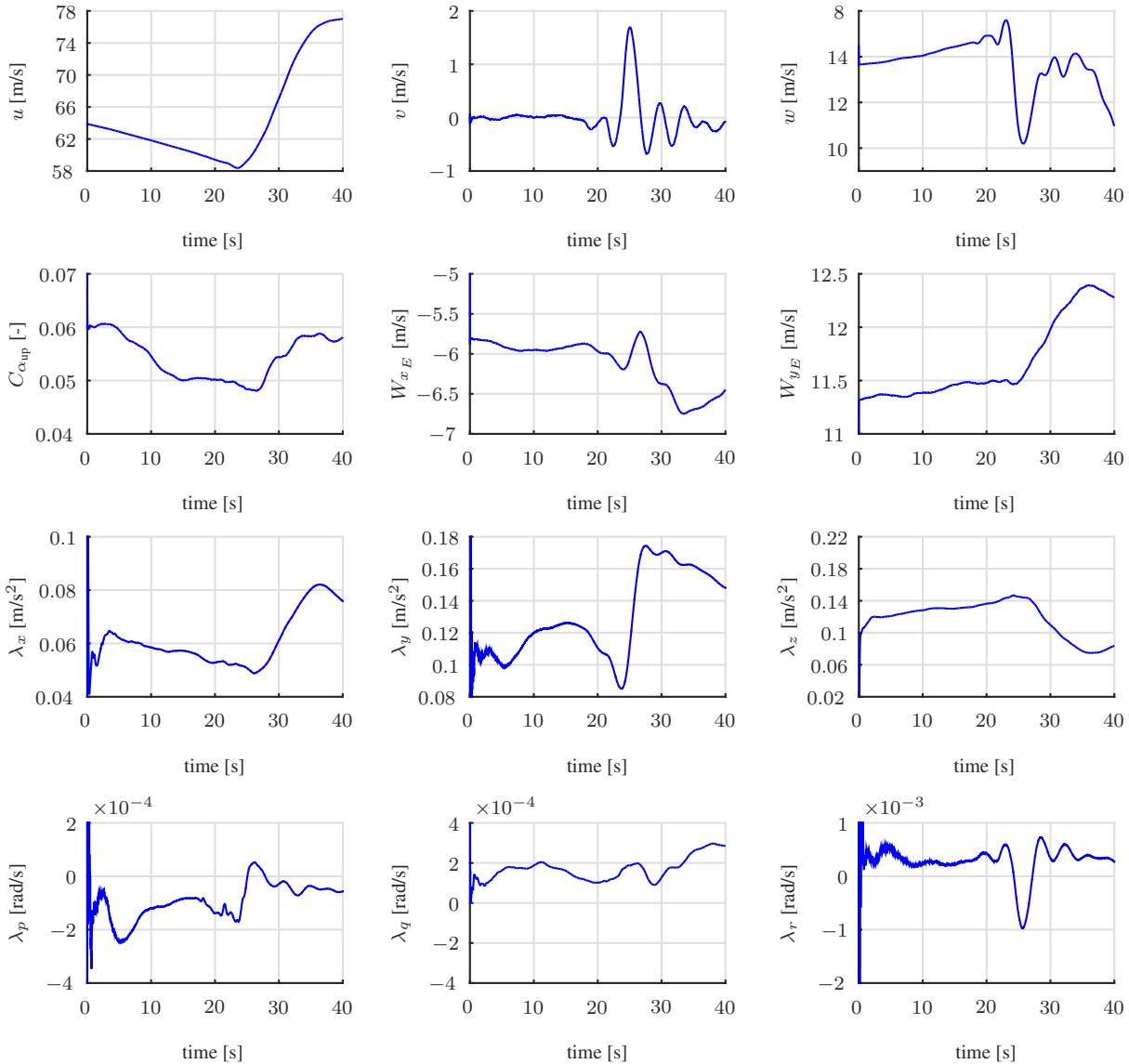


Figure 20. Example of the estimated state for a stall occurring at $t = 23$ s.

V.B. Aerodynamic Model

In Figures 21, 22 and 23 the estimated parameters can be found as a function of altitude. As can be noticed, with the quasi-steady stall approaches the parameters for the lift can be estimated rather well, as indicated by the Cramer-Rao lower bounds. The values for the drag (Figure 22) and moment coefficients (Figure 23), however, show a lot more variance. This indicates that the parameters for the drag- and moment coefficients are more uncertain.

Another method for validating the parameters is comparing them to the literature. In Table 4 the flow separation point parameters from other literature is given. The found values of a_1 and α^* as given in Figure 21 correspond to the

found values in literature. The value of τ_2 on the other hand (with $\bar{c} = 2.09$ m and $V_{\text{stall}} = 59$ m/s), is approximately three times higher than the values found in literature.

Table 4. Flow separation point parameters from for other aircraft and airfoils.

Parameter	Embraer AT-26 Xavante ⁴³	VFW-614 ³⁸	C-160 ³⁸	NACA 0015 ⁴⁴
a_1	25	14.9	25.7	-
α^* [rad]	0.25	0.34	0.36	-
$\tau_1 \frac{\bar{c}}{V}$ [s]	-	15.6	14.5	0.52
$\tau_2 \frac{\bar{c}}{V}$ [s]	-	4.45	3.46	4.5

Other values that were found were the semi-empirical coefficients C_{D_X} and C_{m_X} . For the Embraer AT-26 Xavante, at Mach = 0.4, these are 0.2 and -0.08 respectively.⁴³ The value of C_{D_X} for the VFW-614 is 0.22 and for the C-160 approximately 0.40.³⁸ The values that were found, as shown in Figures 22 and 23 are approximately 0.2 and -0.12 for C_{D_X} and C_{m_X} , respectively, corresponding well with the values found in literature.

Lastly for the Embraer AT-26 Xavante a control effectiveness ($C_{m_{\delta_e}}$) was found of approximately -0.4,⁴³ which corresponds to the value found in Figure 21.

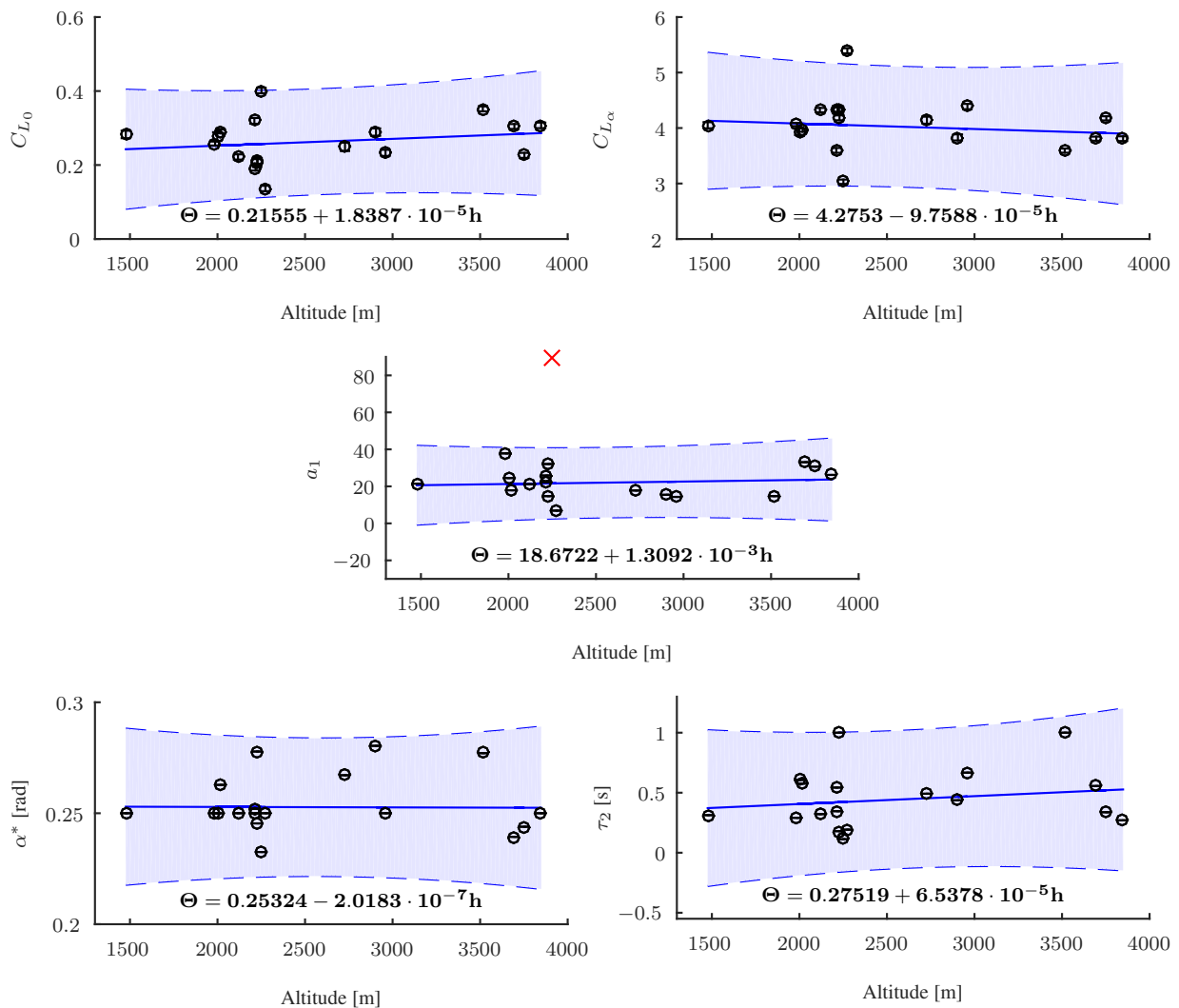


Figure 21. Lift coefficient parameters estimated from the flight test data.

Another interesting statistic is the cross correlation between parameters. A high absolute value (close to 1 or -1) indicates that the parameters are closely coupled. A high value, according to Klein et al.,³⁷ has an absolute value greater than 0.9. Looking at Tables 5, 6 and 7 the only highly coupled parameters are the constant term ($C_{L_0}, C_{D_0}, C_{m_0}$)

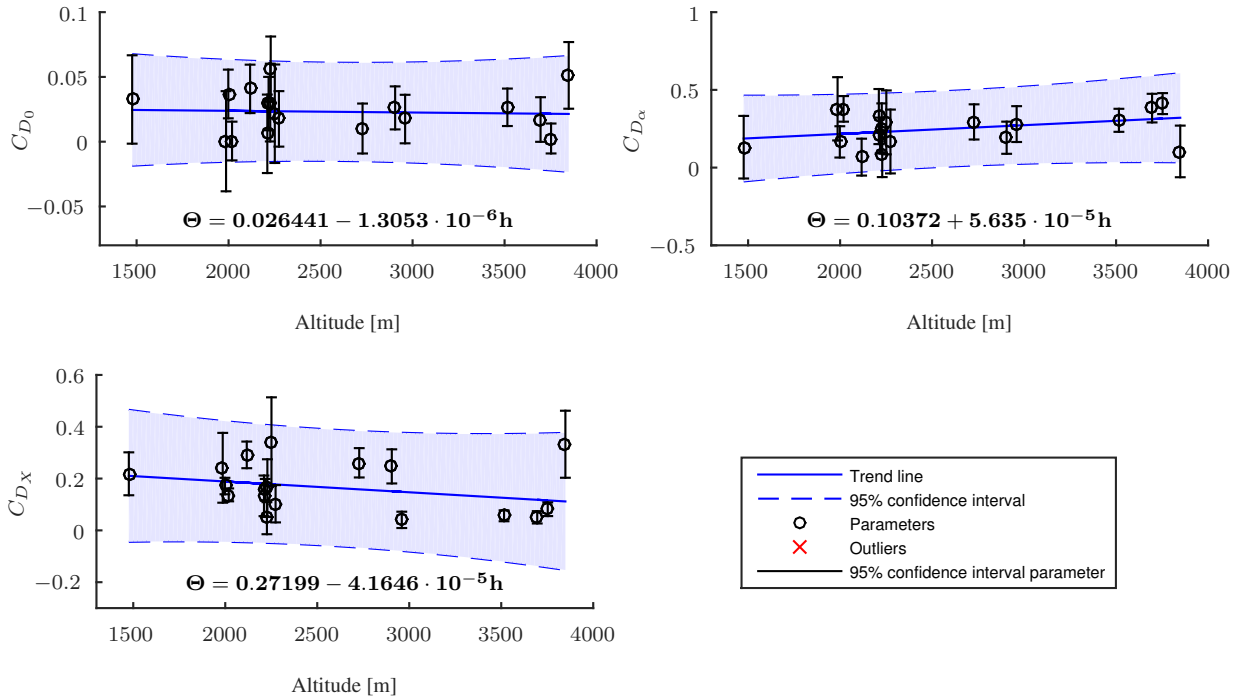


Figure 22. Drag coefficient parameters estimated from the flight test data.

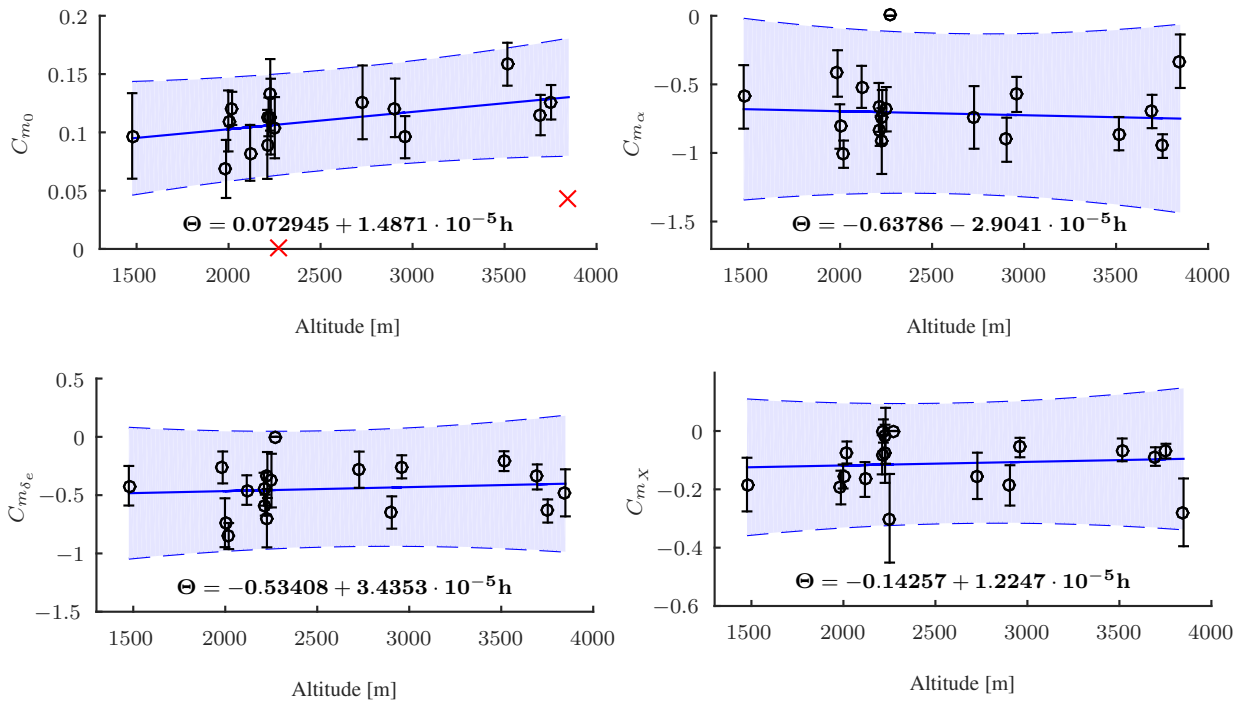


Figure 23. Moment coefficient parameters estimated from the flight test data.

and the angle-of-attack term. This high negative correlation between the intercept ($C_{L_0}, C_{D_0}, C_{m_0}$) and the slope ($C_{L_\alpha}, C_{D_\alpha}, C_{m_\alpha}$) is a result of the fact that all the data points are far away from $\alpha = 0$. When the slope increases somewhat the intercept has to decrease, otherwise the estimated output would be too large. To decrease this correlation more dynamic input maneuvers, such as an elevator doublet could be used. Another method could be to include a dynamic maneuver at a lower angle-of-attack. These two methods increase the angle-of-attack range, resulting in a lower correlation between the slope and the intercept. All the other values are below a value of 0.9, indicating that these parameters can be sufficiently dissociated.³⁷

Table 5. Correlation matrix for the parameters corresponding to the lift coefficient.

	C_{L_0}	C_{L_α}	a_1	α^*	τ_2
C_{L_0}	1.0000	-0.9916	-0.0214	0.0104	-0.0185
C_{L_α}	-	1.0000	-0.0187	-0.0134	0.0185
a_1	-	-	1.0000	-0.2361	-0.4101
α^*	-	-	-	1.0000	-0.3089
τ_2	-	-	-	-	1.0000

Table 6. Correlation matrix for the parameters corresponding to the drag coefficient.

	C_{D_0}	C_{D_α}	C_{D_X}
C_{D_0}	1.0000	-0.9794	0.2953
C_{D_α}	-	1.0000	-0.4424
C_{D_X}	-	-	1.0000

Table 7. Correlation matrix for the parameters corresponding to the moment coefficient.

	C_{m_0}	C_{m_α}	$C_{m_{\delta_e}}$	C_{m_X}
C_{m_0}	1.0000	-0.8576	0.0236	0.4242
C_{m_α}	-	1.0000	0.4513	-0.3580
$C_{m_{\delta_e}}$	-	-	1.0000	-0.2415
C_{m_X}	-	-	-	1.0000

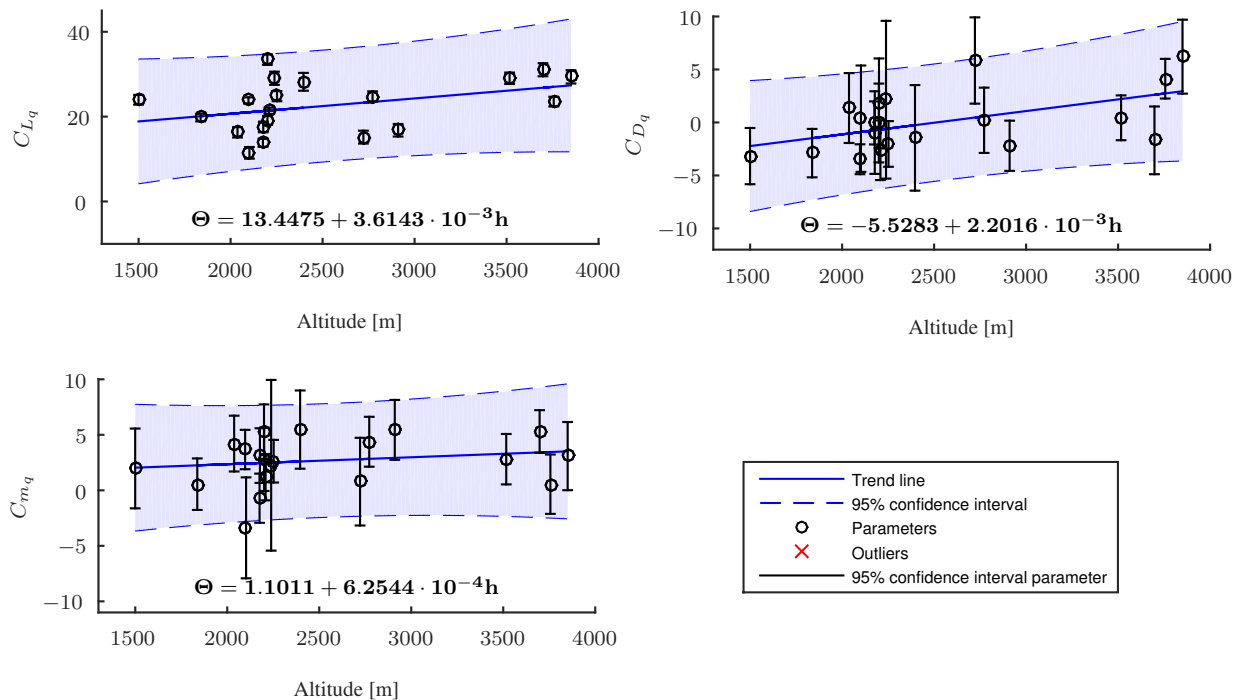


Figure 24. Estimated aerodynamic derivatives related to the pitch rate.

The aerodynamic terms related to the influence of pitch rate were omitted from the look up tables. The main reason for doing so is because the terms: C_{D_q} and C_{m_q} could not be estimated from quasi-steady stalls. As shown in Figure 24, these parameters have a large variance. The worst case is for the drag coefficient, in which half of the time the value is negative and the other half positive. Another interesting fact is that C_{m_q} is estimated to be positive, whereas a negative value is expected, as is the case for the Embraer AT-26 Xavante.⁴³ The only pitch rate parameter that could be identified is C_{L_q} , the reason for not doing so is threefold. First it will make the aerodynamic model structure less clear by using a pitch rate term in one equation and not in the others. Secondly the coefficient of determination on the identification set hardly improves. Without the pitch rate term the average coefficient of determination on the

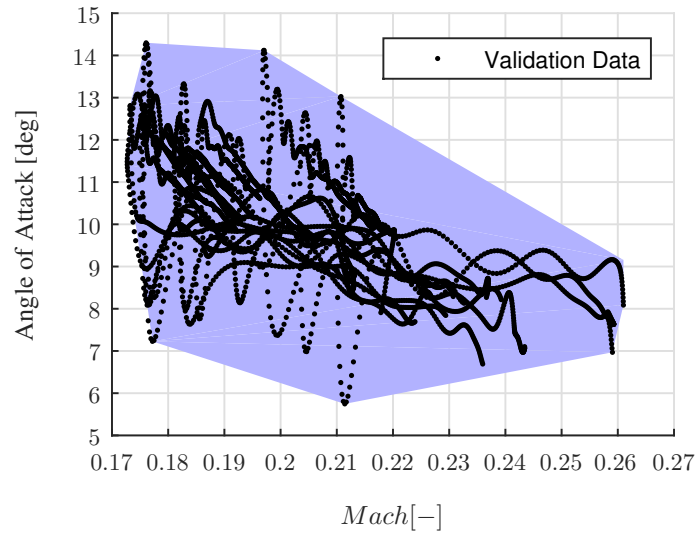


Figure 25. An overview of the validation data in the Mach vs. angle-of-attack plane.

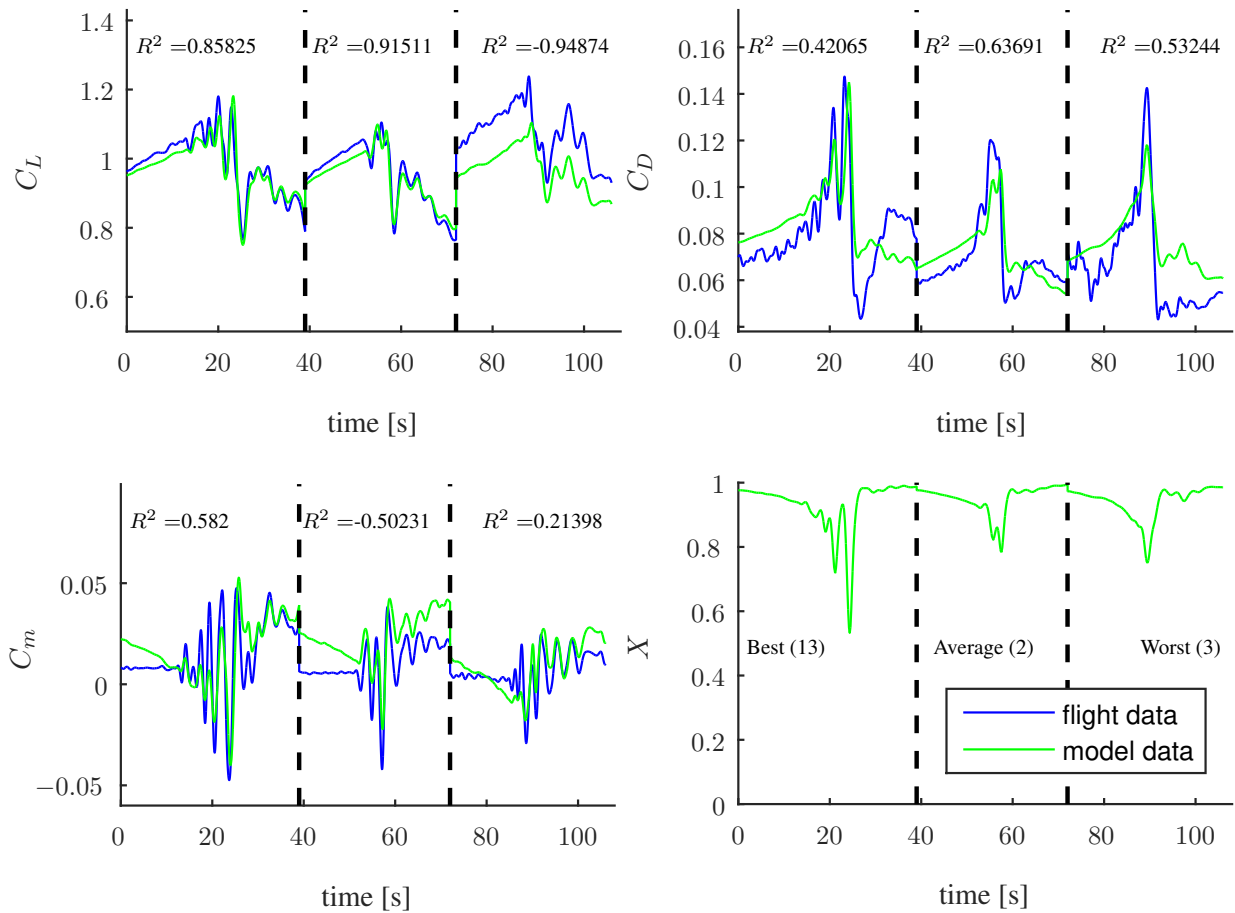


Figure 26. Validation data for the dimensionless forces and moment. The numbers on the bottom right (i.e., 13, 2 and 3), indicate the validation set index as shown in Figure 3.

identification set is **0.8712**, whereas with the pitch rate term this value is **0.8891**. Lastly in the flow separation point both a_1 and, more directly, τ_2 influence the influence of the angle-of-attack rate. The angle-of-attack rate and pitch rate, also with quasi-steady stalls, are still very much correlated. Since the angle-of-attack rate is used, indirectly a damping term such as C_{L_q} is used.

Good practice is that identified models should also be validated using data which was not used for model fitting. During this research approximately 75% of the data was used for parameter estimation and 25% for validation. The validation data in the Mach vs. angle-of-attack plane is shown in Figure 25, indicating where the flight model is validated. Three of the validation sets are shown in Figure 26, indicating a best fit, average fit and the worst case fit. As shown the general trends between the flight data and the model data correspond. The lift coefficient shows the best fit. The drag coefficient is somewhat overestimated, but except for the best case it shows a better fit than for the pitch moment coefficient. The pitching moment is difficult to predict with quasi-steady stall maneuvers. One possible method of increasing the moment coefficient model is to use dynamic stall maneuvers, with e.g., elevator doublets during approach to stall. The dynamic stalls that were executed for this research, i.e. a symmetrical stall using a pull-up maneuver with a load factor of 1.3g, did not show better fitting on the identification data compared to the quasi-steady stalls.

V.C. Buffet Model

The stall buffet is obtained by Fourier analysis of the acceleration signals, to obtain the periodograms. These power spectral density estimates can be used to fit frequency response functions for the stall buffet model. The PSD of the raw data and the fitted models, for both the vertical and lateral acceleration, are shown in Figure 27. The stall buffet in vertical direction has one dominant frequency around 12 Hz, whereas the lateral acceleration has two peak frequencies: one at 10 Hz and one at 6 Hz. The coefficient of determination (R^2) for the vertical buffet model is **0.976** and for the lateral acceleration **0.771**. In Tables 8 and 9 the parameters for the vertical and lateral buffet models can be found. As can be noticed the Cramer-Rao lower bounds are rather low, which together with a high value of the coefficient of determination indicates that the model is a good fit.

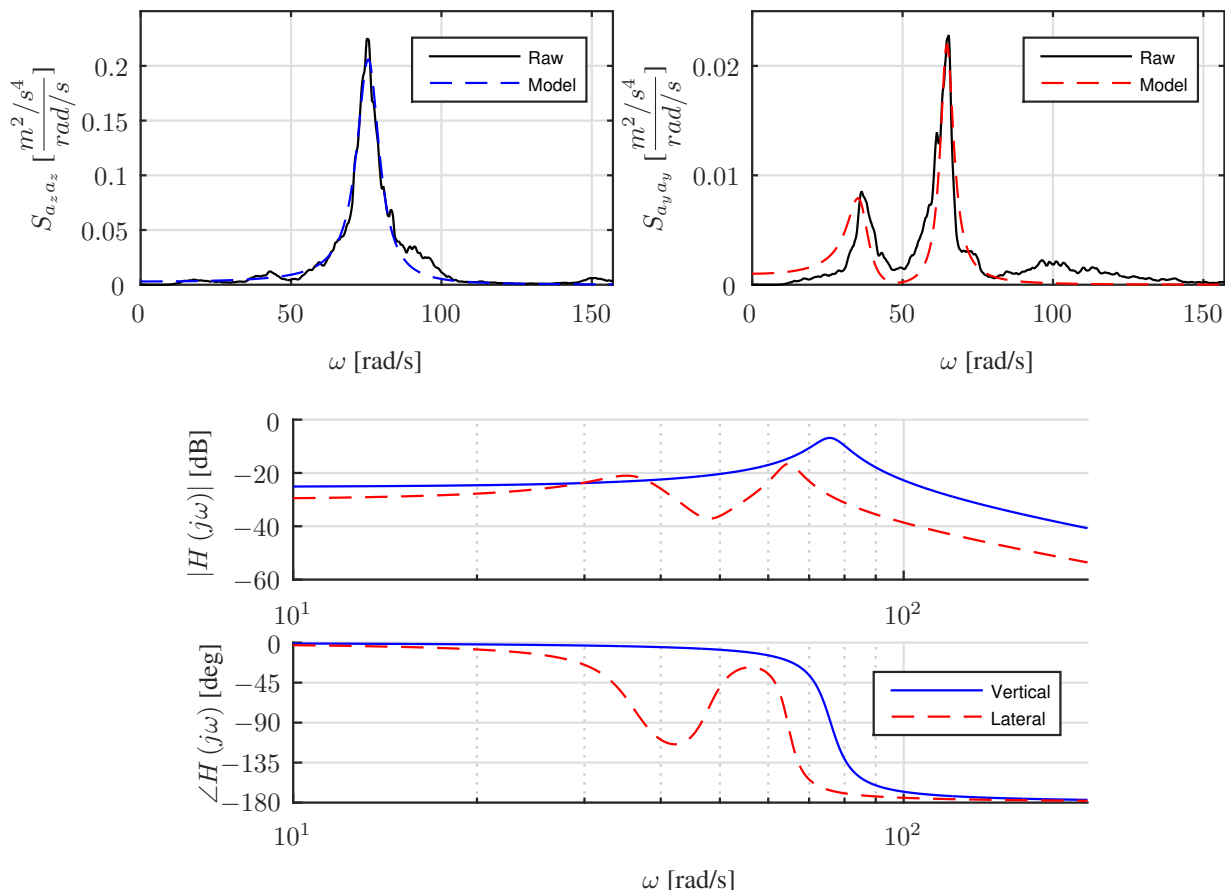


Figure 27. Stall buffet model estimation results.

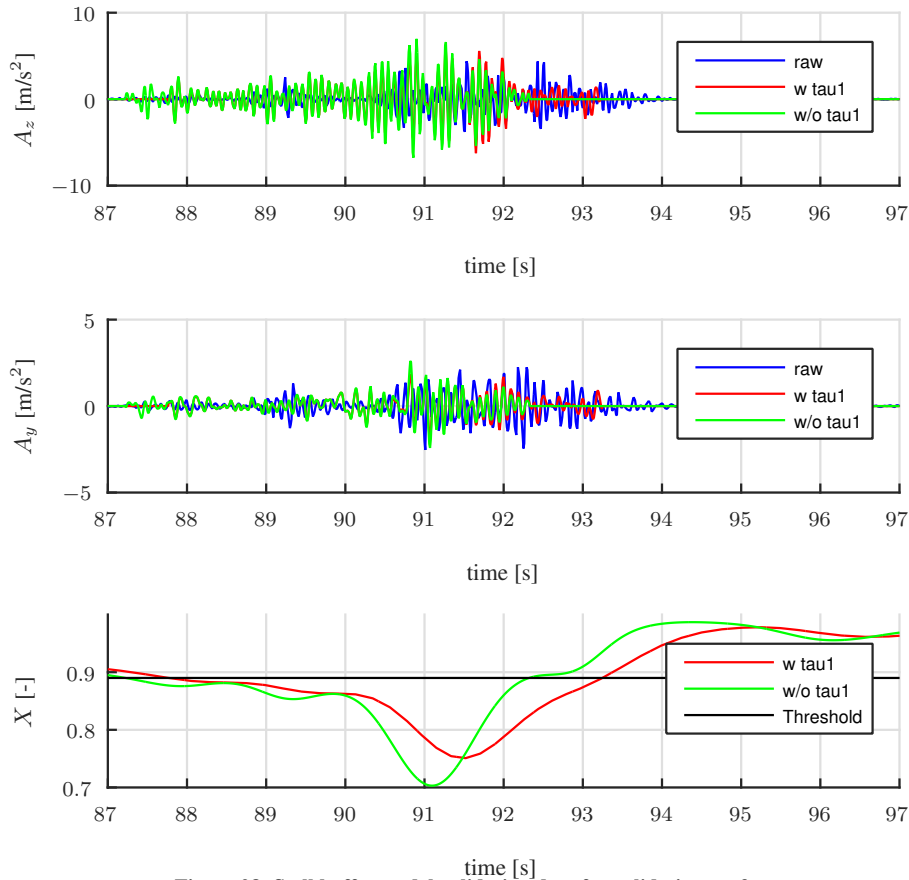
Table 8. Parameters for the vertical acceleration

unit	β	σ	$\frac{\sigma(\beta)}{\beta} \times 100$
H_0 [-]	0.05	3.57e-04	0.65
ω_0 [rad/s]	75.92	2.83e-02	0.04
Q_0 [-]	8.28	9.15e-04	0.01

Table 9. Parameters for the lateral acceleration

unit	β	σ	$\frac{\sigma(\beta)}{\beta} \times 100$
H_0 [-]	0.02	1.15e-03	5.86
ω_0 [rad/s]	36.43	2.43e-01	0.67
Q_0 [-]	4.19	1.77e-02	0.42
H_1 [-]	0.01	1.39e-04	1.14
ω_1 [rad/s]	64.71	2.70e-02	0.04
Q_1 [-]	11.99	1.13e-03	0.01

Next to the frequency-domain data, it is interesting to look at a time history plot for the stall buffet. In Figures 28 and 29, two validation sets for the stall buffet are shown. Both figures show that the stall buffet without transient effect stops prematurely compared to flight data. When the transient effect is included a prolonged buffet can be seen, which matches the flight data better. Therefore it is suggested to use the flow separation point as threshold level, instead of the angle-of-attack, Because the latter variable does not have such a transient effect. Using the flow separation point thus allows for a more accurate representation of the stall buffet cue. It can, however, also be noticed that in Figure 29 the stall buffet model acts too late compared to the measured stall buffet from flight data. Indicating that also this method of calculating the stall buffet is still not perfect.

**Figure 28. Stall buffet model validation data for validation set 3.**

The value of τ_1 for this particular aircraft was estimated to be **0.6253**. Looking at Table 4 this value matches closely with values found in literature. The threshold value for the onset flow separation point was estimated to be **0.89**. If the flow separation value gets below this particular level then the buffet cue will be turned on.

VI. Discussion

This paper investigated the extent to which key characteristics of aerodynamic stall – i.e., aerodynamic flow separation and stall buffets – can be modeled from flight test data collected for quasi-steady stall maneuvers. Previous research has shown promising results for modeling stalls using an approximation of Kirchhoff’s flow separation the-

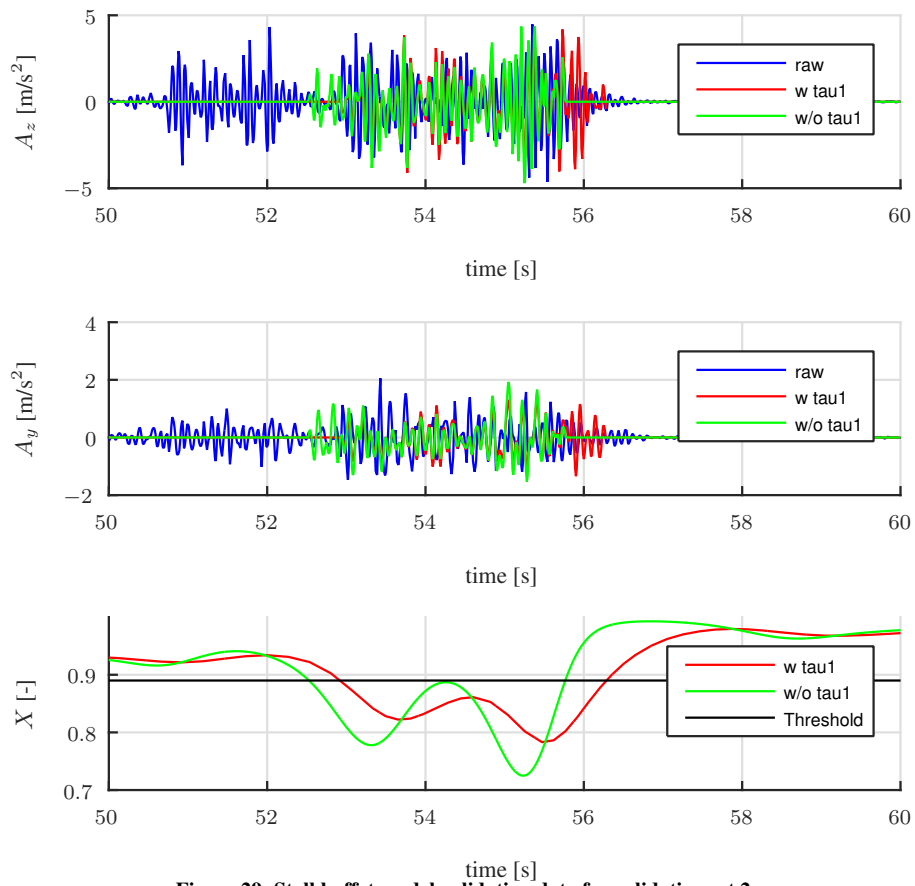


Figure 29. Stall buffet model validation data for validation set 2.

ory.^{24,38,39} However, so far in this research most often use is made of special types of flight test maneuvers, such as doublets, to ensure identifiability of the stall dynamics.

Research institutes and companies, however, might have quasi-steady stall data available, whereas for dynamic data extra flight tests have to be scheduled. This research identifies which stall characteristics can be modeled using quasi-steady maneuvers. This might reduce the cost of stall modeling, in case the most important stall characteristics can be replicated.

Due to the lacking measurement of a side slip measurement, a pseudo-beta was introduced. This increased the quality of the FPR, but only for longitudinal maneuvers. This lack of side slip, however, also means that only the longitudinal forces and moments could be predicted. Although a lateral component could be modeled by calculating the lift and drag of both wings separately, characteristics such as the reduced aileron and rudder control effectiveness could not be predicted. To predict the lateral forces and moments, a baseline model is used.³¹ From this baseline model the roll damping C_{l_p} could be removed, since by calculating the forces for both wings separately this effect is already included. The effect of reduced aileron and rudder effectiveness could be modeled by reducing the forces and moment generated by the aileron and rudder respectively. The reduction of the elevator effectiveness, on the other hand, could be estimated. On average a value of -0.4 was found for $C_{m_{\delta_e}}$, whereas the baseline model has a value of approximately -1.3.³¹

During this research a large negative correlation between the intercept (C_{L_0} , C_{D_0} , C_{m_0}) and the slope (C_{L_α} , C_{D_α} , C_{m_α}) was found. This is caused by the fact that all values of the angle-of-attack are far from zero and only limited variation in alpha is experienced around the stall angle. This problem could be solved by: 1) Applying a dynamic maneuver at a lower angle-of-attack, where C_{L_α} is constant and 2) a dynamic maneuver around the critical angle-of-attack. The first maneuver will give some extra data closer to zero angle-of-attack, whereas the second maneuver gives more variation in angle-of-attack around the stall point. The dynamic stalls that were performed for this research did not show better fitting on the identification data, compared to the quasi-steady symmetrical induced stalls.

The proposed method of estimating the value of τ_1 from the stall buffet data is promising. It was found, however, that due to the randomness of the input signal of the stall buffet, the estimated value of τ_1 varied a little bit depending on the random seed. To make the estimation of τ_1 independent of this random seed multiple runs were done. The found values of all these runs were then averaged to obtain a single value for τ_1 . It would be interesting to see how this proposed method compares to estimating τ_1 from highly dynamic stall maneuvers.

Another interesting research field would be to look at a global aerodynamic model, for example using multivariate splines.³⁴ To identify stability derivatives related to the rotational rates, however, dynamic stall maneuvers must be conducted that are designed specifically for aerodynamic model identification. Such dynamic stall maneuvers are also more likely to improve the fidelity of the moment coefficient. During this research four dynamic stalls were captured, each in a different configuration. This, however, was not enough to properly validate such dynamic stall maneuvers. Single maneuver evaluation is also unusable,²³ therefore during this research the stalls were concatenated in groups of three, which was found to be a good number for parameter estimation. Another interesting study would be to investigate the effect of flaps and landing gear on stall characteristics such as the stall buffet or hysteresis effect.

Lastly, apart from stall model identification, it would be interesting to fly the current identified model in a full motion simulator. This could be done to obtain a subject matter rating on the stall model, based on quasi-steady stalls. Especially since the moment coefficient could not be estimated accurately, therefore the pitch angle does not match closely to the measured pitch angle in flight. On top of that it could be investigated which stall characteristics are the most important for stall recovery training.

VII. Conclusion

In this work an aerodynamic stall model is created based on flight data. It was found that the UKF was suitable for flight path reconstruction techniques. Furthermore it was found that for longitudinal maneuvers it is better to use a pseudo-beta, i.e., a side slip angle modeled as a zero-mean white noise signal, than no side slip observation. It was also found that the vertical wind component (W_{zE}) was not observable and that the fuselage upwash component on the angle-of-attack ($C_{\alpha_{up}}$) and unknown wind component in the angle-of-attack measurement (C_{α_0}) were highly correlated. Therefore, without additional excitation, such as a stall, no clear distinction could be made between these two variables. Hence C_{α_0} was left out of the state as well.

Furthermore, it was found that the hysteresis effect is identifiable using quasi-steady stall maneuvers. The aerodynamic parameters related to the pitch rate, however, showed large variances, indicating that these parameters were not identifiable, except for C_{L_q} . In fact C_{D_q} was found to be both positive and negative and C_{m_q} was estimated to be positive, whereas one would expect a negative value.

The validation sets showed that the identification of the lift coefficient showed the best results, followed by the drag coefficient. The parameters regarding the moment coefficient were difficult to estimate in general, using quasi-steady stall maneuvers. The simulated pitch angle did not match closely to the pitch angle in flight, given the same initial conditions and inputs. The dynamic stalls that were performed for this research did not show better fitting on the identification data, compared to the quasi-steady symmetrical induced stalls.

Although the transient effect could not be identified directly with the other parameters, a method was found to estimate τ_1 from the stall buffet. Using these accelerations a stall buffet model could be created, based on frequency domain analysis. It was found that the altitude does not have a significant effect on the magnitude or frequency of this buffet. The largest buffet accelerations were found to be in z-direction, the second largest in y-direction. The buffet in x-direction on the other hand is negligible. The flow separation point was used as main driver for the stall buffet, both as threshold and as scaling factor. This resulted in a more accurate representation of the stall buffet than using the angle-of-attack.

In conclusion, characteristics such as stall hysteresis and stall buffets are identifiable using quasi-steady stall maneuvers, without a side slip measurement. Other effects such as a degradation in lateral-directional stability or the degradation in control effectiveness were not identifiable from the current flight data, but can be obtained following the same methodology for stall flight test data including control excitation.

Acknowledgements

The authors would like to thank Dr. Sunjoo Advani for his extensive feedback and motivating comments on the research described in this paper.

References

- ¹NTSB, “Annual Review 2013 – Data and Statistics,” 2013.
- ²Lambregts, A. A., Nesemeier, G., Wilborn, J. E., and Newman, R. L., “Airplane Upsets: Old Problem, New Issues,” *Proceedings of the AIAA Modeling and Simulation Technologies Conference and Exhibit, Honolulu (HI)*, No. AIAA-2008-6867, Aug. 2008.
- ³Crider, D. A., “Accident Lessons for Stall Upset Recovery Training,” *Proceedings of the AIAA Guidance, Navigation, and Control Conference, Toronto, Canada*, No. AIAA-2010-8003, Aug. 2010.
- ⁴FAA, “FAA 14 CFR PART 121: Qualification, Service, and Use of Crewmembers and Aircraft Dispatchers; Final Rule,” 2013.
- ⁵Anonymous, “Stall and Stick Pusher Training,” Advisory Circular 120-109, U.S. Department of Transportation, Federal Aviation Administration, Aug. 2012.
- ⁶Advani, S. K. and Schroeder, J. A., “Global Implementation of Upset Prevention & Recovery Training,” *Proceedings of the AIAA Modeling and Simulation Technologies Conference, San Diego (CA)*, No. AIAA-2016-1430, 2016.
- ⁷J. V. Foster and K. Cunningham and C. M. Fremaux and G. H. Shah and E. C. Stewart and R. A. Rivers and J. E. Wilborn and W. Gato, “Dynamics Modeling and Simulation of Large Transport Airplanes in Upset Conditions,” *AIAA Guidance, Navigation, and Control Conference and Exhibit*, No. AIAA-2005-5933, American Institute of Aeronautics and Astronautics (AIAA), San Francisco, CA, USA, Aug 2005.
- ⁸Advani, S. K., Schroeder, J. A., and Burks, B., “What Really Can Be Done in Simulation to Improve Upset Training?” *Proceedings of the AIAA Modeling and Simulation Technologies Conference, 2-5 August 2010, Toronto, Canada*, No. AIAA-2010-7791, 2010.
- ⁹Advani, S. K. and Field, J., “Upset Prevention and Recovery Training in Flight Simulators,” *Proceedings of the AIAA Modeling and Simulation Technologies Conference, Portland (OR)*, No. AIAA-2011-6698, 2011.
- ¹⁰M. J. O’Rourke and J. N. Ralston and J. W. Bell and S. F. Lash, “PC-Based Simulation of the F-16/MATV,” *Modeling and Simulation Technologies Conference*, American Institute of Aeronautics and Astronautics (AIAA), New Orleans, LA, USA, Aug 1997, pp. 481–489.
- ¹¹J. Kay and J. N. Ralston and S. F. Lash, “Development of Non-Linear, Low-Speed Aerodynamic Model for the F-16/VISTA,” *22nd Atmospheric Flight Mechanics Conference*, American Institute of Aeronautics and Astronautics (AIAA), New Orleans, LA, USA, Aug 1997, pp. 822 – 830.
- ¹²C. J. O’Connor and J. N. Ralston and T. Fitzgerald, “Evaluation of the NAWC/AD F/A-18 C/D simulation including database coverage and dynamic data implementation techniques,” *21st Atmospheric Flight Mechanics Conference*, American Institute of Aeronautics and Astronautics (AIAA), San Diego, CA, USA, Jul 1996, pp. 735 – 745.
- ¹³G. N. Malcolm, “Rotary-Balance Experiments on a Modern Fighter Aircraft Configuration at High Reynolds Numbers,” *12th Atmospheric Flight Mechanics Conference*, American Institute of Aeronautics and Astronautics (AIAA), Snowmass, CO, USA, Aug 1985, pp. 462 – 482.
- ¹⁴Groen, E. L., Ledegang, W., Field, J., Smaili, M. H., Roza, Z. C., Fucke, L., Nooij, S., Goman, M., Mayrhofer, M., Zaichik, L. E., Grigoryev, M., and Biryukov, V., “SUPRA – Enhanced Upset Recovery Simulation,” *Proceedings of the AIAA Modeling and Simulation Technologies Conference, Minneapolis (MN)*, No. AIAA-2012-4630, 2012.
- ¹⁵N. B. Abramov and M. G. Goman and A. N. Khrabrov and E. N. Kolesnikov and L. Fucke and B. Soemarwoto and H. Smaili, “Pushing Ahead - SUPRA Airplane Model for Upset Recovery,” *AIAA Modeling and Simulation Technologies Conference*, American Institute of Aeronautics and Astronautics (AIAA), Minneapolis, MN, USA, Aug 2012.
- ¹⁶Abramov, N., Goman, M., Khrabrov, A., Kolesnikov, E., Sidoryuk, M., Soemarwoto, B., and Smaili, M. H., “Aerodynamic Model of Transport Airplane in Extended Envelope for Simulation of Upset Recovery,” *Proceedings of the 28th International Congress of the Aeronautical Sciences, Brisbane, Australia*, 2012.

- ¹⁷Murch, A. M. and Foster, J. V., "Recent NASA Research on Aerodynamic Modeling of Post-Stall and Spin Dynamics of Large Transport Airplanes," *Proceedings of the 45th AIAA Aerospace Sciences Meeting and Exhibit, Reno (NV)*, No. AIAA-2007-463, 2007.
- ¹⁸Y. Nie and E. van Kampen and Q. P. Chu and T. Kier and G. Looye, "Geometry Based Quick Aircraft Modeling Method for Upset Recovery Applications," *Proceedings of the AIAA Modeling and Simulation Technologies Conference*, American Institute of Aeronautics and Astronautics (AIAA), Kissimmee, FL, USA, Jan 2015.
- ¹⁹T. T. Teng and T. S. Zhang and S. Liu and P. R. Grant, "Representative Post-Stall Modeling of T-tail Regional Jet and Turboprop Aircraft for Flight Training Simulator," *AIAA Modeling and Simulation Technologies Conference*, American Institute of Aeronautics and Astronautics (AIAA), Kissimmee, FL, USA, Jan 2015.
- ²⁰D. R. Gingras and J. N. Ralston and R. Oltman and C. Wilkening and R. Watts and P. Desrochers, "Flight Simulator Augmentation for Stall and Upset Training," *AIAA Modeling and Simulation Technologies Conference*, American Institute of Aeronautics and Astronautics (AIAA), Jan 2014.
- ²¹J. A. Schroeder and J. Bürki-Cohen and D. A. Shikany and D. R. Gingras and P. Desrochers, "An Evaluation of Several Stall Models for Commercial Transport Training," *AIAA Modeling and Simulation Technologies Conference*, No. AIAA-2014-1002, American Institute of Aeronautics and Astronautics (AIAA), National Harbor, MD, USA, Jan 2014.
- ²²E. A. Morelli and K. Cunningham and M. A. Hill, "Global Aerodynamic Modeling for Stall/Upset Recovery Training Using Efficient Piloted Flight Test Techniques," *AIAA Modeling and Simulation Technologies (MST) Conference*, American Institute of Aeronautics and Astronautics (AIAA), Boston, MA, USA, Aug 2013.
- ²³S. Weiss and H. Friehe and E. Plaetschke and D. Rohlf, "X-31A System Identification Using Single-Surface Excitation at High Angles of Attack," *Journal of Aircraft*, Vol. 33, No. 3, May 1996, pp. 485–490.
- ²⁴J. N. Dias, "Unsteady and Post-Stall Model Identification Using Dynamic Stall Maneuvers," *AIAA Atmospheric Flight Mechanics Conference*, American Institute of Aeronautics and Astronautics (AIAA), Dallas, TX, USA, Jun 2015.
- ²⁵Cessna Aircraft Company, Wichita, Kansas, USA, *Operating Manual Mdoel 550 Citation II, Unit -0627 And On*, 1990.
- ²⁶B. O. S. Teixeira and L. A. B. Tôres and P. Iscol and L. A. Aguirre, "Flight path reconstruction –A comparison of nonlinear Kalman filter and smoother algorithms," *Aerospace Science and Technology*, Vol. 15, No. 1, Jan 2011, pp. 60–71.
- ²⁷E. A. Wan and R. van der Merwe, "The Unscented Kalman Filter for Nonlinear Estimation," *Proceedings of the IEEE 2000 Adaptive Systems for Signal Processing, Communications, and Control Symposium (Cat. No.00EX373)*, Institute of Electrical & Electronics Engineers (IEEE), Alta, UT, USA, Oct 2000, pp. 153 – 158.
- ²⁸S. Feng and R. Murray-Smith, "Fusing Kinect Sensor and Inertial Sensors with Multi-rate Kalman Filter," *IET Conference on Data Fusion & Target Tracking 2014: Algorithms and Applications*, Institution of Engineering and Technology (IET), Apr 2014, pp. 1 – 8.
- ²⁹M. Laban, *On-Line Aircraft Aerodynamic Model Identification*, PhD thesis, Delft University of Technology, Faculty of Aerospace Engineering, Delft, The Netherlands, May 1994.
- ³⁰A. V. Oppenheim and R. W. Schaffer, and J. R. Buck, *Discrete-time Signal Processing (2Nd Ed.)*, Prentice-Hall, Inc., Upper Saddle River, NJ, USA, 1999.
- ³¹van den Hoek, M. A., de Visser, C. C., and Pool, D. M., "Identification of a Cessna Citation II Model Based on Flight Test Data," *Proceedings of the 4th CEAS Specialist Conference on Guidance, Navigation & Control, Warsaw, Poland*, 2017.
- ³²R. J. M. Bennis, *Non-linear State Estimation Techniques with Application to Dynamic Modelling of Angle of Attack Vane from Cessna Citation II Flight Data*, MSc thesis, Delft University of Technology, Faculty of Aerospace Engineering, Delft, The Netherlands, Aug 1998.
- ³³P. M. T. Zaal and D. M. Pool and M. M. van Paassen and M. Mulder, "Comparing Multimodal Pilot Pitch Control Behavior Between Simulated and Real Flight," *Journal of Guidance, Control, and Dynamics*, Vol. 35, No. 5, Sep 2012, pp. 1456–1471.
- ³⁴C. C. de Visser, *Global Nonlinear Model Identification with Multivariate Splines*, PhD thesis, Delft University of Technology, Faculty of Aerospace Engineering, Delft, The Netherlands, Jun 2011.
- ³⁵B. L. Walcott and M. J. Corless and S. H. Zak, "Comparative study of non-linear state-observation techniques," *International Journal of Control*, Vol. 45, No. 6, Jun 1987, pp. 2109–2132.
- ³⁶J. A. Mulder and J. K. Sridhar and J. H. Breeman, "AGARD Flight Test Techniques Series. Volume 3. Identification of Dynamic Systems-Applications to Aircraft. Part 2. Nonlinear Analysis and Manoeuvre Design.," Tech. Rep. 2, DTIC Document, 7 Rue Ancelle, 92200 Neuilly-sur-Seine, France, 1994.
- ³⁷V. Klein and E. A. Morelli, *Aircraft System Identification: Theory and Practice*, American Institute of Aeronautics and Astronautics (AIAA), Jan 2006.
- ³⁸D. Fischenberg, "Identification of an unsteady aerodynamic stall model from flight test data," *20th Atmospheric Flight Mechanics Conference*, American Institute of Aeronautics and Astronautics (AIAA), Baltimore, MD, USA, Aug 1995, pp. 138 – 146.
- ³⁹D. Fischenberg and R. V. Jategaonkar, "Identification of Aircraft Stall Behavior from Flight Test Data," *Proceedings of the RTO SCI Symposium on System Identification for Integrated Aircraft Development and Flight Testing*, No. RTO MP-11 in , German Aerospace Center (DLR), Braunschweig, Germany, Mar 1999, pp. 17–1 – 17–8.
- ⁴⁰J. A. Mulder and W. H. J. J. van Staveren and J. C. van der Vaart and E. de Weerd and C. C. de Visser and A. C. in 't Veld and E. Mooij, *Lecture Notes AE3202: Flight Dynamics*, Delft University of Technology, Delft, The Netherlands, Mar 2013.
- ⁴¹J.J. Moré and D.C. Sorensen, "Computing a Trust Region Step," *SIAM Journal on Scientific and Statistical Computing*, Vol. 4, No. 3, Sep 1983, pp. 553–572.
- ⁴²T. F. Coleman and Y. Li, "An Interior Trust Region Approach for Nonlinear Minimization Subject to Bounds," *SIAM J. Optim.*, Vol. 6, No. 2, May 1996, pp. 418–445.
- ⁴³J. N. Dias, "High Angle of Attack Model Identification with Compressibility Effects," *AIAA Atmospheric Flight Mechanics Conference*, American Institute of Aeronautics and Astronautics (AIAA), Kissimmee, FL, USA, Jan 2015.
- ⁴⁴M. Goman and A. Khrabrov, "State-Space Representation of Aerodynamic Characteristics of an Aircraft at High Angles of Attack," *Journal of Aircraft*, Vol. 31, No. 5, sep 1994, pp. 1109–1115.